Quantification of Tomographic Incompleteness in Cone-Beam Reconstruction

Rolf Clackdoyle, Frederic Noo

This article has been accepted for publication in a future issue of this journal, but has not been fully edited. Content may change prior to final publication. Citation information: DOI 10.1109/TRPMS.2019.2918222, IEEE Transactions on Radiation and Plasma Medical Sciences

Quantification of Tomographic Incompleteness in Cone-Beam Reconstruction

Rolf Clackdoyle and Frédéric Noo

***Abstract*—For situations of cone-beam scanning where the measurements are incomplete, we propose a method to quantify the severity of the missing information at each voxel. This incompleteness metric is geometric; it uses only the relative locations of all cone-beam vertices with respect to the voxel in question, and does not apply global information such as the object extent or the pattern of incompleteness of other voxels. The values are non-negative, with zero indicating "least incompleteness," i.e. minimal danger of incompleteness artifacts. The incompleteness value can be related to the severity of the potential reconstruction artifact at the voxel location, independent of reconstruction algorithm. We performed a computer simulation of x-ray sources along a circular trajectory, and used small multi-disk test-objects to examine the local effects of data incompleteness. The observed behavior of the reconstructed test-objects quantitatively matched the precalculated incompleteness values. A second simulation of a hypothetical SPECT breast imaging system used only 12 pinholes. Reconstructions were performed using analytic and iterative methods, and five reconstructed test-objects matched the behavior predicted by the incompleteness model. The model is based on known sufficiency conditions for data incompleteness, and provides strong predictive guidance for what can go wrong with incomplete cone-beam data.**

I. Introduction

Cone-beam tomography is the basis for image reconstruction theory and algorithms in the fields of X-ray Computed Tomography (CT) using area detectors and Single Photon Emission Computed Tomography (SPECT) with pinhole collimators. In X-ray CT and in pinhole SPECT, a good first-order mathematical model is to treat the measurements as cone-beam (CB) projections. The vertex of the cone corresponds physically to the x-ray source in CT applications, and corresponds to the pinhole for SPECT applications. Cone-beam theory and algorithms have been extensively studied for conventional circular and helical scanning, as well as more exotic vertex trajectories such as the saddle, or circle-and-line and variants [1], [2], [3], [4], [5], [6]. If the CB projections are not truncated, then much more general trajectories can be handled, with reliable reconstruction possible [7], [8] in the region satisfying Tuy's condition [1] and stable reconstruction impossible elsewhere [2]. However, if the CB vertices do not follow a piecewise smooth trajectory or if the CB projections are truncated, then much of current CB theory does not apply. Methods using Hilbert transforms and derivatives of the projections can avoid the truncation issues [5], [6] but they have complicated non-local requirements involving the object support and line segments of Hilbert values (see, for example, the case of helical cone-beam tomography with transaxial truncation [9]). There remain many potential CB scanning geometries which lie outside current CB reconstruction theory.

In practice, all scanners supply only a finite number of projections so the vertex trajectory is replaced by a finite set of vertex locations which, strictly-speaking, can never satisfy Tuy's condition. Stationary pinhole SPECT scanners provide a more extreme case where a dozen or so pinholes might be positioned in space with no suggestion of an underlying trajectory. Very little literature exists on the problem of CB tomography from a finite number of vertices. Barrett and Gifford [10] used the concept of a Fourier cross-talk matrix to analyze vertex configurations along a helical path. Their approach could be extended to general vertex configurations but it treats recovery in a global way, and does not appear to be easily modified to handle the variable recoverability of Fourier coefficients throughout an extended field-of-view. There is a body of mathematics literature dealing with recovery of object singularities (such as sharp changes or boundaries) from a finite number of vertices. For example, Quinto [11] identifies visible and invisible singularities in a single cone-beam projection. However, in the limiting case of an infinite collection of vertices satisfying Tuy's condition, these theories only predict that all singularities of the object can be recovered, and we are interested in full tomographic recovery of the density function. Broadening our perspective to include parallel-beam projections but restricting to the two-dimensional (2D) case, the work of Rattey and Lindgren [12] identifies minimal angular sampling of the projections (interwoven with a minimal detector sampling) in order to recover objects of a given size and essential bandwidth. Natterer has similar results for the fan-beam geometry [13], and Desbat has extended these ideas to the case of cone-beam tomography for vertices along a circle [14]. These results can be readily inverted to define a maximum bandwidth which can be recovered from a finite number of vertices but they rely heavily on *uniform* angular sampling and are not powerful enough to address our problem. The idea of linking up vertices to create a Tuy complete trajectory was discussed in [15] and [16], and these ideas led also to direct (analytic) algorithms for reconstruction from arbitrary vertex configurations. Unfortunately, no quantitative link was made between the value of required to convert a finite number of vertices into a Tuy complete set and

This work was partially supported by the U.S. National Institutes of Health under grant number R21 CA82843, and partially supported by the French Agence Nationale de la Recherche under grants ANR-12-BS01-0018 ("DROITE") and ANR-17-BS01-0018 ("ROIdoré") from the Agence Nationale de la Recherche.

R. Clackdoyle is with the TIMC-IMAG laboratory (CNRS UMR 5525), Grenoble, France. E-mail: rolf.clackdoyle@univ-grenoble-alpes.fr

F. Noo is with the Utah Center for Advanced Imaging Research, University of Utah, Salt Lake City, USA. E-mail: frederic.noo@hsc.utah.edu

This article has been accepted for publication in a future issue of this journal, but has not been fully edited. Content may change prior to final publication. Citation information: DOI 10.1109/TRPMS.2019.2918222, IEEE Transactions on Radiation and Plasma Medical Sciences

the reconstruction quality obtained or obtainable using this approach. Other works on reconstruction from a finite number of projections can be found, but they generally address parallel geometries and are not suitable for CB problems.

For completely general vertex trajectories/sets and arbitrary projection truncation, current CB reconstruction theory is not sufficiently advanced to answer simple questions on which voxels can be reliably reconstructed and which regions of the object have been insufficiently sampled by the 3D Radon transform and therefore cannot be reliably reconstructed. In this context, regions of reliable reconstruction means that the reconstruction will be correct in a certain region for all possible objects that are being scanned. (The point is, even in cases of severe data incompleteness, there can still be certain objects that reconstruct correctly. An extreme example is just one parallel projection; if the object density is constant in the integration direction, then it can be perfectly reconstructed.)

In this work, we describe a simple measure of local incompleteness, with the property that it quantitatively describes how poorly a certain test object is expected to be reconstructed in principle (independent of reconstruction algorithm). This measure was previously presented in a different context in conference proceedings papers [17], [18], [19]. The scope is broader here, to include truncated CB projections, and more detailed studies are provided.

The incompleteness metric that we propose here has the noteworthy feature that for each voxel, an incompleteness value is assigned to each direction. We use the symbol $I(x,\theta)$ to represent the incompleteness value at 3D location x, in the direction $\theta \in S^2$. Different directions have different degrees of incompleteness as we will discuss in the theory section and illustrate in the simulations section. Two features we stress here are the incompleteness notion, rather than completeness, and the directional aspect at the voxel level.

There have been various descriptions of local completeness metrics in the literature, based on known necessary conditions for CB reconstruction. Our incompleteness metric is based on those same conditions, which become sufficient conditions for incompleteness. This distinction is essentially semantics, but we feel that a value of "zero incompleteness" is less likely to be mis-interpreted than "100% completeness" when, in both cases, the local conditions do not necessarily ensure reliable reconstruction (as will be discussed below). We will consistently emphasize that our metric, $I(x,\theta)$, provides a lower bound (i.e. a minimal level) of incompleteness. The various existing completeness metrics are discussed in the following section.

II. Background

As discussed below, various completeness conditions as well as one incompleteness condition appear in the literature. The completeness conditions are all based on (a) Tuy's condition [1], or on (b) 3D Radon inversion formulas [20] or on (c) a local version of Orlov's condition [21]. Tuy's sufficiency conditions for CB reconstruction are that every plane intersecting the object must contain at least one vertex point. Furthermore, none of the CB projections can be truncated, and it is assumed that the support (the extent) of the object is known. This condition is essentially the same as the 3D Radon condition that all plane integrals intersecting the object must be known [3]. Finally, in the limiting case where the vertex trajectory lies at infinity, the CB projections become parallel, and Tuy's condition becomes Orlov's sufficiency condition: the set of projection directions, when traced on the unit sphere, must intersect every great circle [22].

In 2001, we presented a completeness condition for a finite collection of non-truncated CB projections in the context of pinhole SPECT, and defined a directional condition at each point x, denoted $R(x,\theta)$ [19]. Following Tuy's condition, for each point x, we consider all planes through x. For the plane with normal vector θ we look for the CB vertex which comes closest to the plane. If a vertex lies on the plane, then $R(x,\theta) = 0$, and if not, we look for the closest vertex v_i to the plane, not in the sense of distance to the plane, but in the sense of the (positive) angle made between the plane and the line connecting x to v_i. We called this angle ψ_i and we assigned $R(x,\theta) = \tan\psi_i$. Note that for a finite set of vertices, $R(x,\theta)$ will be non-zero for almost all planes (almost all θ). We discuss this definition further in the Section III.

In 2003, Metzler published a "sampling completeness" condition SC for helical pinhole SPECT [23], but it can clearly be applied to any CB vertex trajectory. In this work, each voxel was considered as the center of its own "Orlov sphere" and the projection of the vertex trajectory onto this sphere was called a vantage curve. Orlov's condition requires that all great circles intersect this vantage curve, although true data completeness is only ensured if all projections are parallel and non-truncated. Nevertheless, the percentage of all possible great circles intersecting the vantage curve was used for the SC value at each voxel. This completeness measure is not applicable to finite sets of vertices, so the CB trajectory is always considered to be "continuous." In a related publication [22], the Orlov sphere description is linked to a local form of Tuy's condition, and an algorithm for evaluating the SC measure in practice is described in detail.

Other completeness measures in the literature follow the spirit of these two early contributions. There has been increased interest in this topic, particularly in recent years with half a dozen papers appearing since 2010.

In 2010, Stopp *et al* proposed an "image recording quality measure" $q(x)$ for applications in limited-angle X-ray scanning [24]. The quality measure $q(x)$ was similar in spirit to an averaged version of $R(x,\theta)$ described above. Again using ψ_i to denote the minimum angle made by the ith vertex with respect to the plane through x with normal θ, the quantity $q(x)$ was defined by averaging $|\cos\psi_i|$ over all normal directions θ. The maximum possible value of 1.0 would mean that Tuy's condition is satisfied at x, and smaller values represent poorer quality measures. The results were compared with RMS errors from SART reconstructions of the Shepp-Logan phantom.

Also in 2010, Lin and Meikle explored 3D sampling requirements in the context of pinhole SPECT with circular and helical trajectories, including projection truncation [25], [26]. They used the SC measure in the context of local Orlov spheres, and were primarily investigating situations of 100%

This article has been accepted for publication in a future issue of this journal, but has not been fully edited. Content may change prior to final publication. Citation information: DOI 10.1109/TRPMS.2019.2918222, IEEE Transactions on Radiation and Plasma Medical Sciences

SC in all voxels. Their simulations showed artifacts in regions where SC was less than 100%.

In 2011, Dai *et al* also use a "sampling completeness" criterion to compare scanning orbits in pinhole SPECT [27]. Their criterion, called SCP, is the SC measure for each voxel expressed as a percent. They suggested that an SCP threshold value of 95 would be suitable for reconstructions in practice, and they compared the number of voxels attaining this threshold for circular and helical scanning orbits.

In 2012, Liu *et al* used their "completeness map" concept to evaluate various cardiac CT scanning modes, including circular and helical scanning. They justified their data completeness number in terms of 3D Radon transform theory, and arrived at the percentage of planes passing through the point x that are measured from CB vertices along the trajectory. This criterion turns out to be mathematically equivalent to SC. In addition, the authors are careful to point out that "a 100% completeness number is a necessary condition to reconstruct the corresponding point ... not a sufficient condition" [28] and they point to the 3D interior problem [20] as an example where unique reconstruction is not possible even though a 100% completeness map exists. The authors also make the following statement, which is relevant to our work presented below: "it is difficult to establish the image quality that corresponds to a completeness level that is less than 100%".

In 2015, a paper addressing data completeness in multiplexing multi-pinhole SPECT appeared [29]. The completeness criterion was the Metzler model using Orlov sphere and a cleverly chosen set of vantage directions that were identified as the effectively non-multiplexed directions. Five pinhole scanning configurations were examined and data completeness was identified as either 100"% or incomplete. For data complete situations where the authors "do not expect any artifacts," subsequent simulation studies verified that image quality was consistent with the data completeness criterion.

A weakness common to all these works [19], [23], [24], [26], [27], [28], [29] is that they can not be used as a general data-*completeness* measure. This fact has been explicitly mentioned in several of these works. In the case where none of the CB projections are truncated (a rare situation, in practice) these completeness measures are reliable. However, if some projections are truncated then a calculated completeness of 100% can be misleading. The difficulty is that general completeness conditions are not determined only by the local (voxel-level) behavior of measured line integrals in two-dimensions (fan-beam) or three-dimensions (cone-beam). Some global information of the measured data configuration is also required, such as knowledge of the object extent (the "object support") and the pattern of measurement lines through a neighboring region of voxels that includes the object boundary. A well-known specific example is described by the interior problem [20] where all CB projections are measured but are all completely truncated (no part of the object boundary is visible in any CB projection view). In this case all seven listed works would indicate 100% completeness for the "interior" points that are visible in the CB projections, but reconstruction theory states that unique image reconstruction is not possible for these points (unless strong *a priori* information is available). Further discussion of general CB data-completeness theory can be found in [30], [6].

On the other hand, an effective *incompleteness* condition can be achieved at the voxel level, based on a converse of Tuy's condition, due to Finch: stable image reconstruction is not possible (irrespective of reconstruction algorithm) at a voxel location if there exists a plane through that contains no CB vertex [2].

This approach to defining an incompleteness condition was recently adopted in [31]. A non-directional "local Tuy condition" was defined at each voxel as the worst (largest) value of $|\sin\psi_i|$ taken over all directions $\theta \in S^2$ with ψ_i defined earlier as the smallest angle with respect to the plane normal to θ subtended at the voxel by all CB vertices. The local Tuy value was convincingly validated using simulations with a phantom consisting of a grid of small concentric spheres.

Here, we propose an incompleteness value $I(x,\theta)$ at each voxel, which indicates the degree of incompleteness. The key point made by Finch was that a function which varies quickly between two parallel planes passing through a neighborhood of x cannot be reconstructed if all measured lines pass through both planes. What is missing is a CB vertex on the plane passing through x and generates lines to separate (pass between) the two planes. We suggest a measure that quantifies this incompleteness by identifying the closest CB vertex to the plane in question. A novel feature of this work is that we provide concrete examples of "what can go wrong?" and "how badly?" in terms of the magnitude of the incompleteness parameter. We illustrate the efficacy of our definition using computer simulations.

III. Theory

Cone-beam projections $g(a_i,\cdot)$ are defined as collections of ideal line-integrals

$$g(a_i,\alpha) = \int_0^\infty f(a_i + t\alpha)\, dt \tag{1}$$

where a_i represents the location of the ith CB vertex, $f(x)$ is the intensity at x of the physical parameter being scanned ("the object function"), and $\alpha \in S^2$ is a unit vector specifying the direction of the ray leaving the vertex a_i and passing through the object. Figure 1 illustrates the geometry of a single CB projection. The two independent parameters of the vector α are determined by the intersection point of the ray on the detector. By removing considerations of detector resolution and sampling, we have reduced the problem to considering only the geometric configuration of the cone vertices with respect to the 3D locations x of interest.

Given a collection of (unordered) CB vertices $\{a_1, a_2, \ldots a_n\}$, we define the local directional incompleteness metric $I(x,\theta)$ by

$$I(x,\theta) = \min\{\tan\psi_i : i = 1,2,\ldots n\} \tag{2}$$

where x represents the location in the imaging field, $\theta \in S^2$ is a unit vector indicating the diretion being sampled, and

$$\sin\psi_i = |(a_i - x)\cdot\theta| \,/\, ||a_i - x|| \tag{3}$$

This article has been accepted for publication in a future issue of this journal, but has not been fully edited. Content may change prior to final publication. Citation information: DOI 10.1109/TRPMS.2019.2918222, IEEE Transactions on Radiation and Plasma Medical Sciences

defines the angle ψ_i made by the line-of-view from the vertex a_i to location x and the plane perpendicular to θ and passing through x. See fig 2.

We extend this definition in the obvious way when considering a path or trajectory of vertices. If a_λ is the vetex position on a smooth and bounded trajectory parametrized by $\lambda \in [\lambda_1, \lambda_2]$, we define

$$I(x,\theta) = \min\{\tan\psi_\lambda : \lambda \in [\lambda_1, \lambda_2]\} \tag{4}$$

where

$$\sin\psi_\lambda = |(a_\lambda - x)\cdot\theta| \,/\, ||a_\lambda - x||. \tag{5}$$

Note that for both definitions, the angles ψ_i or ψ_λ lie in the range $[0, \pi/2]$, so $I(x,\theta) \in [0,\infty]$. Also, for both definitions, we are only considering the *effective* vertex set or vertex trajectory corresponding to the point x. That is, we only consider those CB vertices for which a measurement line is present from the vertex through the point x. In the case of non-truncated projections, the effective vertices are the same for all points x, but for truncated projections, each point x can have its own characteristic ("effective") sub-collection of vertices.

In the following two subsections, we discuss the definition of $I(x,\theta)$ in the context of existing CB reconstruction theory. We assume no *a priori* information about the unknown object density.

A. Non-truncated CB projections; vertex trajectories

For the case of non-truncated CB projections taken from a vertex trajectory, existing theory tells us precisely where stable reconstruction is possible. It is important to note that part of the object may be reconstructible even though other regions of the object are not. From the local form of Tuy's condition [1], reconstruction is possible at a (small neighborhood of a) point x if every plane passing through (the neighborhood of) x intersects the vertex path. (From now on, "x" implicitly refers to a small neighborhood about the point x.) Conversely, if there are planes passing through x which do not intersect the vertex path, then stable reconstruction at x is not possible in principle, independent of reconstruction algorithm [2].

From the definition of $I(x,\theta)$ we see that if every plane passing through x intersects the source trajectory, then

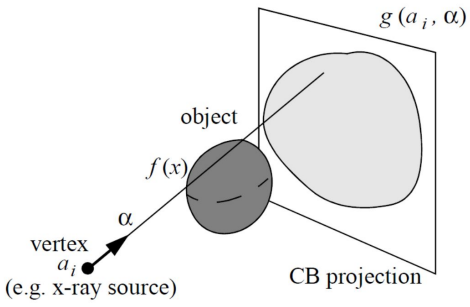

Fig. 1. A cone-beam projection. The cone-beam projection $g(a_i,\cdot)$ is the collection of all line-integrals for rays diverging from the vertex point a_i. If some non-zero line-integrals miss the physical detector, the projection is called truncated.

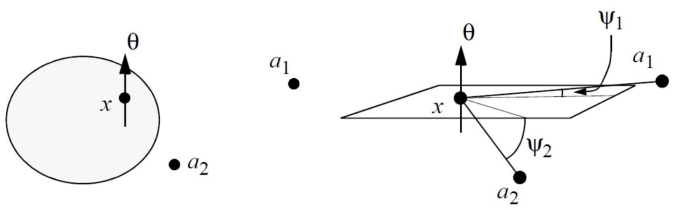

Fig. 2. Example calculation of $I(x,\theta)$. This example involves just two verticies a_1 and a_2 as shown. For the location x and direction θ indicated, ψ_i is angle between the line-of-sight from vertex a_i to x and the plane perpendicular to θ. Here, $I(x,\theta) = \tan\psi_1$.

$I(x,\theta) = 0$ for all θ, which is interpreted as "no incompleteness in any direction" and is in agreement with known theory stating that stable reconstruction is possible at x [1]. Finch's result [2] is a necessary CB completeness condition, and Tuy's result [1] is a sufficient completeness condition (provided no CB truncation occurs). They are respectively sufficient and necessary conditions for incompleteness, so stable CB reconstruction is possible at x if and only if $I(x,\theta) = 0 \quad \forall\theta \in S^2$. Other published completeness / incompleteness measures also demonstrate compatibility with the Tuy-Finch conditions (for non-truncated CB projections). A fast method of determining all reconstructible points is available if the vertex trajectory consists of a single connected (and bounded) component: in this case, the convex hull of the trajectory is exactly the region of reconstructible points [2], [32].

Conversely, if some plane $P_x(\theta)$ passing through x does not contain a CB vertex, then $I(x,\theta) \neq 0$ where θ is the normal vector of the plane in question. Thus any non-zero value of $I(x,\theta)$ indicates a point x for which accurate image reconstruction is not possible. However, this incompleteness measure is more than just a binary indicator of data incompleteness at x because (a) it indicates the direction(s) of the offending plane(s) at x by associating incompleteness to specific planes (on which there is no CB vertex), and (b) it provides a positive value indicating the degree to which the condition is not satisfied in terms of the nearest suitable approximating plane.

For property (a) above, we justify the notion that there is no incompleteness (i.e. $I(x,\theta) = 0$) for all directions θ for which a plane *does* pass through x, even though other directions might fail. Here we appeal to the notion that any object can be represented in the domain of the derivative of the 3D Radon transform. Elements of the domain are conceptually related to planes intersecting the object, and the domain acts locally, meaning that only those elements of the domain corresponding to planes passing through x are needed to recover the object at x [16]. The relevant transform has been called the B-transform [33] or the dipole-sheet transform [34], defined by

$$Bf(\gamma,s) = p(\gamma,s) = \frac{1}{2\pi}\int_{\mathbb{R}^3} f(x)\,\delta'(x\cdot\gamma - s)\,dx \tag{6}$$

where $\gamma \in S^2$, $s \in \mathbb{R}$, and δ' is the derivative of the Dirac delta function defined by $\int h(s)\,\delta'(s_0 - x)\,ds = h'(s_0)$. The inverse B-transform is

$$B^{-1}p(x) = f(x) = \frac{1}{4\pi}\int_{S^2}\int_{\mathbb{R}} p(\gamma,s)\,\delta'(s - x\cdot\gamma)\,ds\,d\gamma. \tag{7}$$

This article has been accepted for publication in a future issue of this journal, but has not been fully edited. Content may change prior to final publication. Citation information: DOI 10.1109/TRPMS.2019.2918222, IEEE Transactions on Radiation and Plasma Medical Sciences

Grangeat's result [3] links CB projections to elements of the B-domain, and more specifically, if a plane intersects the vertex path then the corresponding element of the B-domain can be obtained using Grangeat's formula:

$$\frac{1}{4\pi}\int_{S^2} g(a,\theta)\,\delta'(\theta\cdot\gamma)\,d\theta = p(\gamma,s)|_{s=a\cdot\gamma} \qquad (8)$$

where g is related to f via equation (1), and p is related to f via equation (6). In this sense, planes passing through x which *do* intersect the vertex path are furnishing elements of the B-domain of the object so $I(x,\theta)=0$ (no incompleteness) for those corresponding planes. In particular, if the object decomposition in the B-domain is zero for those planes violating Tuy's condition ($I(x,\theta)\neq 0$ at x) then stable reconstruction can be achieved at x. This situation is in analogy with the familiar concept of limited angle tomography where object reconstruction is possible if the unmeasured frequencies were not present (had zero amplitude) in the object.

For property (b) above, we explain our heuristic approach of using the tangent of the sallest available subtending angle as a measure of the degree of incompleteness in the missing direction (direction θ normal to the plane containing x but not intersecting the vertex path). For a fixed point x and a plane $P_x(\theta)$ not intersecting the vertex path, a *nearest* plane is defined as a plane passing through x whose normal vector makes the smallest possible angle with θ, amongst those planes which do intersect the vertex path. From the definition of equation (5) it can be seen that ψ_λ is this minimum angle. So the degree of incompleteness should be some monotonic (order-preserving) function of ψ_λ. We choose $\tan\psi_\lambda$, based heuristically on the following argument. In considering how the incompleteness would be manifest in image reconstruction at x, we recall that Finch proposed a smooth object function f with a discontinuity along $P_x(\theta)$ [2]. We follow a similar line of thought by considering two small parallel disks separated by a small gap, centered at x and parallel to the plane $P_x(\theta)$. Since $I(x,\theta)\neq 0$, there is no measurement line passing through x and parallel to the disks. Furthermore, there is no measurement line passing through x making an angle of less than ψ_λ with $P_x(\theta)$. If the two disks had unit diameter and were separated by less than $\tan\psi_\lambda$, then any measurement line passing through x would have to traverse both disks, and the gap between them would not be detectable. If the disks were separated by more than $\tan\psi_\lambda$, then there would be measurement lines through x that pass directly between the disks, and would allow the possibility for the center of the disks to be separated in a reconstructed image. The heuristic meaning of $I(x,\theta)$ is the smallest distance that two unit-diameter disks at x with orientation θ can be tomographically separated. We examine this quantitative interpretation in the simulations, sections IV and V below.

B. Non-truncated CB projections; finite vertex sets

We now consider this case of a finite number of vertices, from which all CB projections are nontruncated. In practice, any vertex trajectory must be approximated using a finite collection of vertices and the tacit assumption is that the sampling along the trajectory is sufficiently fine that the "continuous" CB reconstruction theory applies. For the incompleteness measure $I(x,\theta)$, the same assumption can be applied. For a fine sampling of vertices along the trajectory, the definition of equations (2) and (3) will give almost identical values of $I(x,\theta)$ as the definitions (4) and (5). Strictly speaking, there will be many small non-zero values of $I(x,\theta)$ that would have been zero for a true vertex trajectory. However, from knowledge of the sample spacing along the trajectory, a maximum non-zero value due to the sampling effect can be calculated (by examining values of $I(x,\theta)$ for planes that pass between consecutive samples on the trajectory) and used as a threshold to define an "effectively zero" value for $I(x,\theta)$. We do not discuss this point further.

For an arbitrary finite collection of (non-truncated) CB vertices, the situation for a local incompleteness measure remains similar to the case of a vertex trajectory. Suppose there are n CB vertices (and in practice, n can be as small as 20 for modern dedicated cardiac-SPECT cameras). Each point x will have n planes which satisfy Tuy's condition for which the corresponding element of the B-domain will be available using Grangeat's formula. For these planes, equations (2) and (3) will give $I(x,\theta)=0$, and we expect that rapid changes in density at x in the direction θ will be discernible by the CB system. Conversely, where nonzero values, particularly large non-zero values, of $I(x,\theta)$ occur, the system will have difficulty in resolving two small unit disks at x oriented perpendicular to θ, spaced closer than the value of $I(x,\theta)$. Reconstruction methods for arbitrary vertex collections are much less developed than for the standard situation of a vertex trajectory, however, a method called the "Radon Algorithm" takes the approach of building the B-domain and performing the inverse transform to reconstruct the object [15]. This method is analogous method to the Fourier Reconstruction approach in parallel-beam reconstruction theory.

For arbitrary discrete vertex sets, it is useful to consider the convex hull of the vertex locations. Points x inside this convex hull could be considered to lie in a useful reconstruction region because the magnitude of $I(x,\theta)$ will be (conservatively) bounded by a constant multiple of the largest distance between two neighboring vertex points (neighboring in the sense that the separating distance is minimal). Outside the convex hull however, for certain directions θ, the value of $I(x,\theta)$ will grow with increasing distance causing larger and larger holes in the B-domain. However, even at these locations x, well outside the convex hull, some structures of the object will still be reconstructible because there will always be n directions $\{\theta_i\}$ such that $I(x,\theta)=0$ corresponding to the planes that pass through the vertices.

C. Truncated CB projections

For truncated CB projections, general CB reconstruction theory is much less developed. Tuy's condition cannot be applied to truncated projections so theoretically reconstructible regions are not readily identified. On the other hand, Finch still tells us where stable reconstruction is impossible: if a plane intersecting the object doesn't contain a CB vertex, then stable reconstruction will not be possible at object points

This article has been accepted for publication in a future issue of this journal, but has not been fully edited. Content may change prior to final publication. Citation information: DOI 10.1109/TRPMS.2019.2918222, IEEE Transactions on Radiation and Plasma Medical Sciences

in that plane. However, there are now regions of unknown reconstructibility where, for example, each plane through the point contains some CB vertex, but some of these CB projections are truncated. In general, for such locations it is not known if stable reconstruction is possible. (In some special cases, reconstructibility can be established using the tools of differentiated backprojection and Hilbert inversion, but the conditions are complicated and highly specific to the vertex trajectory geometry and the object support [6].) Furthermore, the three-dimensional interior problem tells us that a collection of points $\{x\}$ can have all planes containing CB vertices and yet these points are known to not be uniquely reconstructible; the situation arises when all the corresponding CB projections are truncated in all directions on the detectors.

Translating these facts to the definition of $I(x,\theta)$, for either vertex trajectories or a finite collection of vertices, if there are truncated projections, reconstruction at x is not ensured even if $I(x,\theta) = 0$ for all θ. On the other hand, a non-zero value of $I(x,\theta)$ still means that there are insufficient data to reconstruct density features at x that change rapidly in the θ direction. Furthermore, the value of $I(x,\theta)$ still indicates the closest possible separation of small unit-diameter disks that might be resolved from the data (no matter what reconstruction algorithm is used, barring a priori information). However, for the vertex of minimal ψ_λ that provided the value of $I(x,\theta)$, the CB projection may be truncated so the corresponding point in the B-domain might not be available. In this sense, without further information, non-zero $I(x,\theta)$ indicates a "best possible" case for reconstructibility at x in the θ direction, or equivalently, $I(x,\theta)$ provides a lower bound on the level of incompleteness.

If more information is available concerning the pattern of truncation, then more is known about reconstructibility at points x inside the object. If, for example, a subset of the vertex set (trajectory or discrete vertices) corresponds to non-truncated CB projections, then the meaning of $I(x,\theta)$ becomes more specific if those vertices alone are involved in the calculation. However, the calculated value for $I(x,\theta)$ remains unchanged. For example, if $I(x,\theta) = 0$ at x for all θ, then the fact that (from the vertex subset) no truncated projections were involved tightens the meaning to"stable reconstruction is possible at x" from (in the case of truncated projections) "reconstructibility at x might be possible."

In a substantial extension of the idea of additional information on the pattern of truncation, we introduce the terminology *effectively* non-truncated for the situation where the truncation does not inhibit access to the B-domain. Using Grangeats formula [3] to calculate the B-transform for a plane $P_x(\theta)$, a cone-beam vertex is required for which the corresponding projection values are available at (and in a small neighborhood of) the intersection of $P_x(\theta)$ with the detector. (See figure 3 of [35] where this point is discussed in more detail.) This requirement still allows cone-beam truncation elsewhere in the projection. If all values of $I(x,\theta)$ can be calculated with effectively non-truncated projections, then the same predictive behavior of $I(x,\theta)$ is available as for non-truncated projections.

D. Summary

For non-truncated projections, or for a suitable subset of *effectively* non-truncated projections, the sign of $I(x,\theta)$ merely encodes the results of the known image reconstruction theory of Tuy, Finch, and Grangeat. (By the sign of a nonnegative function we mean zero if the function is zero, and one if the function is non-zero.) In particular, at position x, $I(x,\theta) = 0$ for all θ means that all the required information in the B-domain is available for reliable reconstruction at x. On the other hand, a positive value of $I(x,\theta)$ indicates missing information in the B-domain and that rapid density changes in the θ direction will be poorly reconstructed, independent of the choice of reconstruction algorithm. The magnitude of $I(x,\theta)$ has been put on an heuristic scale to quantify the degree of incompleteness in terms of the expected reconstructibility of two small parallel disks. Since the object under study might not actually contain rapidly changing density in the directions of missing information (the object may have low magnitude components in certain regions of its B-transform), we can regard $I(x,\theta) = 0$ as describing the "worst-case scenario" for the reconstruction of a particular object. On the other hand, this "worst case" can always be realized by considering objects with rapidly changing density at x in the θ direction, such as the disks phantom.

For the general situation of truncated projections, even if the exact pattern of truncation were known, current image reconstruction theory is not generally able to resolve the question of local reconstructibility. The $I(x,\theta)$ value is computed for each vertex for which an integration line to the voxel exists, without regard for truncation of other integration lines in the $P_x(\theta)$ plane. Therefore, a value of zero at x indicates measurements of the corresponding elements of the B-domain which would only be ensured if there was *effectively* no truncation. The same argument applies for non-zero values where the magnitude of $I(x,\theta)$ is assuming the nearest plane (nearest element of the B-domain) is *effectively* not truncated. In both cases, the value of $I(x,\theta)$ is optimistic, and should be regarded as a minimal degree of incompleteness at x. On the other hand, the incompleteness value itself is a "worst-case scenario" for image reconstruction of a particular object, so for general truncated CB projections the definition of $I(x,\theta)$ gives a quantitative description of the minimum degree of incompleteness that would be manifest in the most unfortunate object to be reconstructed (the object whose features align most unfortunately with the pattern of incomplete measurements).

We again emphasize that the calculation of $I(x,\theta)$ involves only the geometry of the CB vertices with respect to the reconstruction point x. All physical effects are assumed to have been corrected perfectly and the detector is assumed to have arbitrarily fine spatial resolution. (This detector assumption is valid on many CB systems where sub-mm sampling exists on the detector whereas the CB vertex spacing is generally much larger than 1 mm.) The values obtained for $I(x,\theta)$ indicate the degree of incompleteness; they are independent of any particular (analytic or iterative) reconstruction algorithm, and assume no a priori information on the object density function.

This article has been accepted for publication in a future issue of this journal, but has not been fully edited. Content may change prior to final publication. Citation information: DOI 10.1109/TRPMS.2019.2918222, IEEE Transactions on Radiation and Plasma Medical Sciences

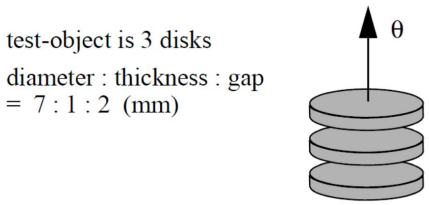

Fig. 3. The test object. The test object consists of three parallel disks of diameter 7 mm, thickness 1 mm, and separated by 2 mm. The axis of the disks indicates the incompleteness direction being tested, θ. The idea is to try to resolve the gap between the disks in the reconstructed images. For the selected dimensions of the disks, the gaps should not be resolvable along the central axis unless $I(x, \theta)$ is less than 0.29.

IV. Simulations

We report here on our simulations studies, whose purpose was to validate the incompleteness model defined by (2)-(3). In our first simulation study, we consider the familiar circular CB geometry for which data incompleteness in planes parallel to the trajectory plane have been known for several decades. (See [36] for a relatively recent study). We use the standard Feldkamp (FDK) reconstruction algorithm [37] for the experimental component of the study. For the second simulation study, we chose an imaging geometry of only 12 CB vertices, for a hypothetical pinhole SPECT imaging system. We study the predicted incompleteness at a handful of locations, and we examine those locations in reconstructed images obtained with both analytic and iterative algorithms.

Following the spirit of the explanations in section III.A, we experimentally examined ideal reconstructed images at various locations x by centering a small test phantom of parallel disks at x and orienting the axis of the disks in some direction θ. By visual inspection of the reconstructed images, we assessed whether the disks were clearly separated, and we compared these results with the predictions given by the formula for $I(x, \theta)$, equations (2)-(3). The disk phantom we used is illustrated in Fig. 3; the radius of the three disks was 3.5 mm, the separation of adjacent disks was 2.0 mm and each disk was 1.0 mm thick. For some studies, the geometry of the disk phantoms was adjusted.

A. Circular vertex trajectory

For the first simulation study, 60 vertices were spaced uniformly along a circle of radius 100 mm. The z-axis corresponded to the axis of rotation, and $z = 0$ was the plane containing the circle of vertices. The detector size was 256 x 256 square pixels each of side 0.33 mm. The detector was positioned at 200 mm from the corresponding vertex, and oriented conventionally, i.e. such that the shortest line segment from the vertex to the detector passed through the center of the vertex circle, and intersected the center of the detector.

To experimentally verify the predictions of our incompleteness model, we placed the small test-objects in three locations along the axis of rotation of the simulated scanner, oriented so that the θ direction was aligned with the rotation axis. The test-objects were considered to be recovered if the reconstructed images completely separated the three disks. For rays to pass between the disks along the central axis of the test-object they would have to be inclined by no more than $\tan^{-1}(2/7)$ from the plane parallel to the disks, so we anticipate that the test objects should not be recoverable unless $I(x, \theta)$ is less than 0.29. The three test-objects were centered respectively at $z = 10$ mm, $z = 29$ mm, and $z = 40$ mm, as illustrated in fig. 4.

Projection data for the 60 vertices were simulated by calculating the intersection length of the line from the vertex to each detector pixel with the phantom, using the mathematical description of the 9 disks comprising the phantom (rather than computing intersections with a voxelized model of the phantom). Note that the detector was large enough to ensure no truncation of the CB projection of the simulated phantom. The reconstructed image was obtained by applying the FDK algorithm [37] to these ideal projection data. The reconstruction array consisted of 200 x 200 x 200 cubic voxels of side 0.2 mm.

The three reconstructed test-objects were examined visually and using plots of the reconstructed intensity values to determine if clean separation of the disks had been achieved in the images. At the three locations x_1 = (0, 0, 10), x_2 = (0, 0, 29), x_3 = (0, 0, 40), the maximum incompleteness value $I(x, \theta)$ is in the direction θ_z = (0, 0, 1) in all cases. For this direction, the incompleteness values are easily calculated from equations (2)-(3): $I(x_1, \theta_z) = 0.10$, $I(x_2, \theta_z) = 0.29$, and $I(x_3, \theta_z) = 0.40$.

Our standard test object (fig. 3) responds to the situation of $I(x, \theta) > 0.29$. For different incompleteness thresholds, the separation and/or diameter of the disks can be varied. We used the same simulated scanner geometry but placed three new test-objects at locations x_1, x_2, x_3 with respective diameters of 12 mm, 10 mm, 7 mm and separations of 1 mm, 2 mm, 4 mm. For the second new test-object centred at x_2, the disk thickness was doubled to 2 mm; all other disks were 1 mm thick. The corresponding incompleteness thresholds for the three new test-objects were 0.083, 0.20, 0.57 respectively.

For general CB geometries, where truncated projections can occur, $I(x, \theta)$ provides a *minimum* incompleteness metric. To illustrate this point we used the same circular geometry of 60 projections, with the standard test object at position x_1, but included a very dense cylinder of height 10 mm and radius 5 mm located at $(50, 10, 15)$ which is outside the field-of-view. This object was completely truncated for 40 of the 60

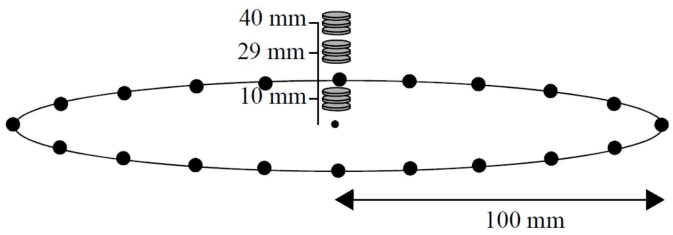

Fig. 4. Details of the circle simulations geometry. Sixty vertices were placed uniformly on a 100 mm radius circle in the x-y plane (only 20 shown). Three test objeects (see fig. 3) were centered on the z-axis at heights of 10 mm, 29 mm, and 40 mm respectively. These locations correspond to $I(x, \theta) =$ 0.10, 0.29, and 0.40 respectively when θ is in the z-direction.

This article has been accepted for publication in a future issue of this journal, but has not been fully edited. Content may change prior to final publication. Citation information: DOI 10.1109/TRPMS.2019.2918222, IEEE Transactions on Radiation and Plasma Medical Sciences

projections; for the other 20 projections, it was "in front" of the test-object for 6 projections, and behind for 14 projections. The density of this cylinder was 9 times that of the disks of the test-object. The standard test-object responds to incompleteness values greater than 0.29 but at location x_1 we have $I(x_1, \theta_z) = 0.10$, so if none of the CB projections were truncated, the disks of the test-object would be resolved. The FDK algorithm was used for reconstruction, even though this algorithm is not suited for transaxially-truncated projections.

Historically, disk phantoms became the standard test object for the circular CB trajectory in 1989 when it was originally suggested by Defrise [38]. The blurring that occurs off the trajectory plane and obscures the separation of the disks is well known. To provide a different (and new) illustration of cone-beam incompleteness artifacts, we also simulated a "shell and bubble" phantom. This phantom consists of the shell component of the standard 3D Shepp-Logan phantom with a small bubble feature placed at the top of the phantom. The defining ellipsoids are given in table 1.

TABLE I
SHELL+BUBBLE PHANTOM; COMPONENT ELLIPSOIDS (IN MM)

Density	a	b	c	x_0	y_0	z_0
2.0	69	90	92	0	0	0
-0.98	66.24	88	87.4	0	0	-1.48
-0.98	4.6	4.6	4.6	0	0	87

Two simulations were performed with this phantom. In both cases, there were 60 projections with corresponding CB vertices evenly spaced along a circle of radius 350 mm lying in the z = 0 plane. The z-axis passed through the centre of the circle. The detector was always 700 mm from the CB vertex, in the opposing position along the trajectory circle, but adjusted in the z-direction to ensure no truncation of the projections. The detector consisted of 128 x 128 square pixels of side 4 mm each. The FDK routine was used for the reconstructions, with 200 x 200 x 200 voxels of side 1.5 mm each. The voxel array was positioned in the same way for both reconstructions, such that the center of the array was 50 mm above the origin of the system.

For the first simulation the phantom was positioned 100 mm above the origin, and for the second simulation, it was positioned 100 mm below the origin. We are interested in the behavior of the reconstruction at the position of the "bubble" so for the first simulation, $x = (0, 0, 187)$, and for the second simulation $x = (0, 0, -13)$. In both cases the incompleteness value at position x was maximized in the $\theta = (0, 0, 1)$ direction with values easily calculated to be $I = 187/350 \approx 0.53$ and $13/350 \approx 0.037$ respectively. We thus anticipate a possible artifact at x for the first simulation but a much smaller artifact for the second simulation.

B. 12 pinhole vertices

A 12-vertex CB geometry was simulated in order to examine more closely the effects of the parameter θ when using $I(x, \theta)$, and to explore an extreme geometry with richer incompleteness properties. Although 12 CB projections might seem artificially low, there are currently clinically operational SPECT cameras in hospitals that use a broadly similar geometry, employing just 19 pinhole projections [39] [40].

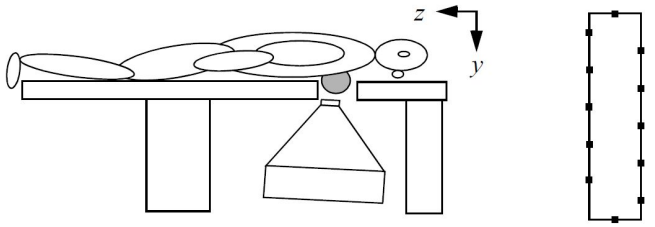

Fig. 5. Schematic of the simulation geometry. A gamma camera with pinhole collimator is successively placed at 12 positions to image the right breast. The 12 vertices (pinhole locations) are irregularly-spaced on a rectangular path (right) on the surface of a hemisphere surrounding the breast. See fig. 6 for projected views of the vertices and breast.

For our 12-vertex example, we simulated a hypothetical multi-pinhole SPECT system for breast imaging. For a phantom, we defined a torso and two breasts using constant density ellipsoids, and we focussed on the right breast with a pinhole system as illustrated in fig. 5. Twelve pinhole projections were considered in a rectangular arrangement located on the surface of an imaginary hemisphere surrounding the right breast as shown in fig. 6. With the assumption that only the right breast was active, none of the 12 CB projections were truncated. We also assumed an ideal detector (perfect spatial resolution) and an arbitrarily small pinhole. We identified 5 locations $(x_1, x_2, \ldots x_5)$ inside the breast and assigned a direction $(\theta_1, \theta_2, \ldots \theta_5)$ to each location. The five pairs are illustrated in fig. 6. Note that locations x_1 and x_5 lie inside the convex hull of the vertices, but the other locations do not. Generally, the incompleteness values will be smaller inside this convex hull as pointed out in Sec. III-A and Sec. III-B.

For this geometry of 12 pinholes, we calculated the full incompleteness function $I(x_i, \cdot)$ for each of these five locations $x_1, x_2, \ldots x_5$. Polar plots were used to display these five functions of θ, as shown in fig. 7. Conceptually, each θ corresponds to a point on the upper unit hemisphere, and one imagines being positioned at the centre of this hemisphere. The z-direction is the centre of the image, corresponding to "looking directly overhead" i.e. the direction $\theta = (0, 0, 1)$. Values along the "equator" correspond to $z = 0$ and are shown along the outer boundary of the circular image, with the x-direction pointing to the right, and the y-direction straight ahead (upwards in the 2D plot). Dark values in the polar plots correspond to values of $I(x, \theta)$ that are close to zero (low incompleteness) and bright values indicate greater incompleteness. As explained in the caption, the 12 dark bands that appear in each polar plot of fig. 7 correspond to the 12 vertices (pinhole locations). The polar plots for x_2, x_3, and x_4 show similar behavior because these locations are quite close to each other, relative to the positions of the vertices. In table 2, we list the values of $I(x_i, \theta_i)$ obtained for the selected directions $\theta_1, \theta_2, \ldots \theta_5$. The positions of these particular values for θ are indicated on the polar plots of fig. 7.

Our model suggests (in agreement with standard theory)

This article has been accepted for publication in a future issue of this journal, but has not been fully edited. Content may change prior to final publication. Citation information: DOI 10.1109/TRPMS.2019.2918222, IEEE Transactions on Radiation and Plasma Medical Sciences

TABLE II
CALCULATED VALUES OF $I(x_i, \theta_i)$

$i=1$	$i=2$	$i=3$	$i=4$	$i=5$
0.0	0.101	0.075	0.400	0.078

that locations x_1 and x_5 exhibit low data incompleteness which depends slightly on their orientation with respect to the available vertices. Locations x_2, x_3, and x_4 (which lie outside the convex hull of the vertices) indicate varying degrees of data incompleteness, that *depend on the orientation* θ under consideration. In particular, the values of $I(x_2, \theta_2)$ and especially $I(x_3, \theta_3)$ are similar to that of $I(x_5, \theta_5)$, so we predict similar levels of image artifact for these situations. On the other hand, $I(x_4, \theta_4)$ is much larger, indicating much more incompleteness, and suggesting noticeable image artifacts in reconstructed images at that location and (unfavorable) orientation.

To experimentally verify the predictions of our incompleteness function, we included in the breast phantom, five small test-objects at the locations x_1 to x_5. The test objects each consisted of 3 parallel disks: thickness 1 mm; diameter 7 mm; separation 2 mm, the same as used for the previous study, see fig. 3. They were oriented so that the axis of the disks lay in the θ direction. As before, the test-objects are considered to be recovered if the reconstructed images completely separate

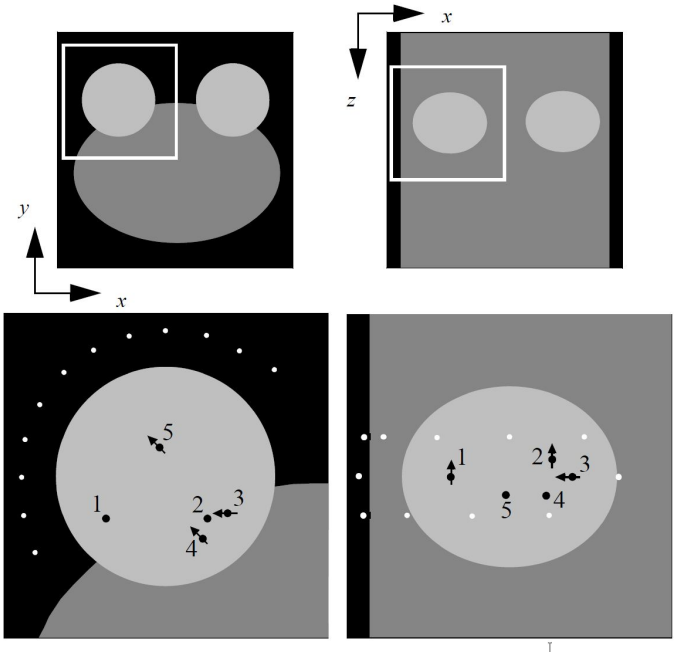

Fig. 6. Details of the simulation geometry. The transverse images (top left) are in standard orientation (viewed from the feet, with patient lying face-up). A parallel projection in the z-direction is shown (bottom left) illustrating the positions of the vertices and the test-objects. Coronal images are shown (top right), with the projection in the y-direction (bottom right). The elliptical torso is visible, but was not used in the simulation. The 5 locations and directions $(x_1, \theta_1) \ldots (x_5, \theta_5)$ under consideration are indicated in black in the projected views; arrows showing the directions are only present when they lie completely in the viewed orientation.

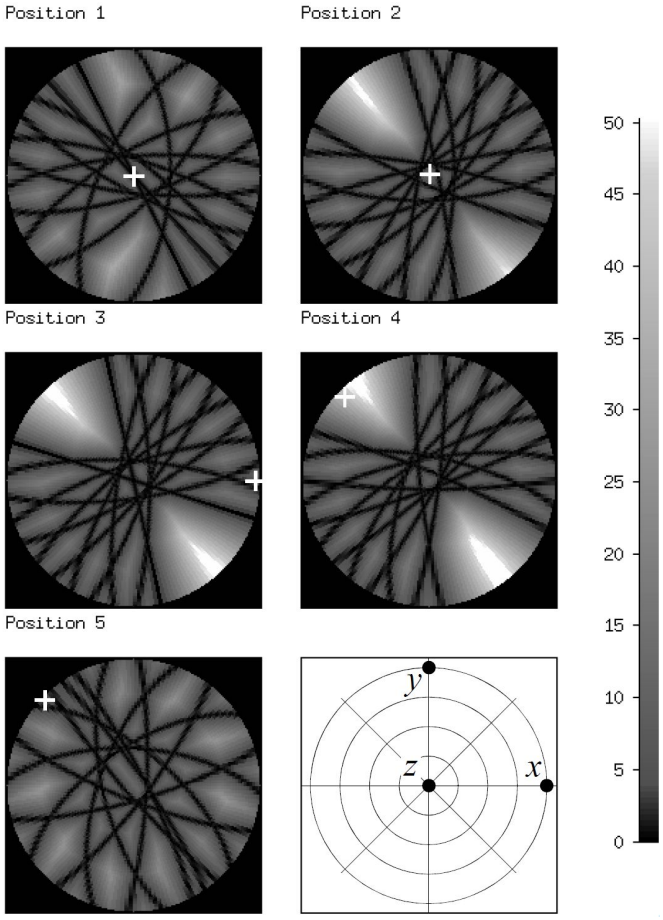

Fig. 7. Polar plots of $I(x, \theta)$ for $x = x_1, x_2, \ldots x_5$. The directions θ are specified as if looking directly in the z-direction ("north pole" as shown bottom right). The $I(x, \theta)$ values have been multiplied by 100. In each plot, the small white "+" indicates θ_i (corresponding to the orientation of the ith test object). The 12 dark bands on each plot are the traces of great circles (on the unit sphere of directions) where each vertex provides "zero incompleteness" (the line-of-sight from the vertex lies perpendicular to θ so the RHS of equation (3) is zero).

the three disks, which we anticipate cannot happen for cases where $I(x, \theta) > 0.28$. Therefore, according to the model, we anticipate test-object 4 will not be recovered, no matter what image reconstruction algorithm is used. Figure 8 shows the five test objects positioned and oriented according to the five computed values $I(x_i, \theta_i)$. The location of one coronal slice and two transverse slices is also indicated, to help interpret the images that the reconstruction algorithm will provide.

Using analytic line-length calculations through the ellipsoidal and disk components, we computed the 12 CB projections of the right breast with activity level 1.0 and the five test-objects with activity level 10.0. These ideal simulated projections were of size 1024 x 1024 with pixel size 0.175 mm x 0.175 mm to avoid detector resolution effects.

Image reconstruction was performed with both analytic and iterative techniques. The scientific objective is to disprove the incompleteness model, which in this case means to try to successfully reconstruct test object 4 (i.e. produce an image with clearly separated disks) which the incompleteness model deems to be impossible.

This article has been accepted for publication in a future issue of this journal, but has not been fully edited. Content may change prior to final publication. Citation information: DOI 10.1109/TRPMS.2019.2918222, IEEE Transactions on Radiation and Plasma Medical Sciences

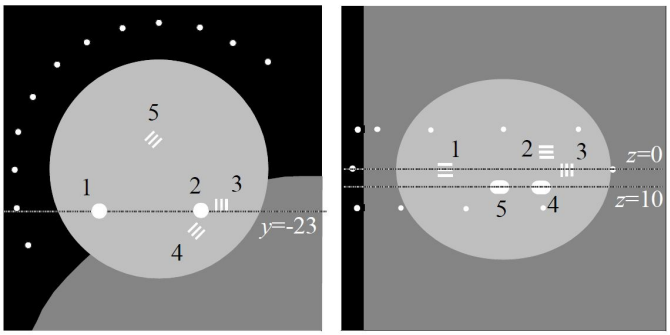

Fig. 8. The five test-objects. Each test-object consists of three parallel disks of diameter 7 mm, thickness 1 mm and separated by 2 mm. The axis of the ith disk was chosen to be θ_i. The idea is to try to resolve the gap between the disks in the reconstructed images. The incompleteness measure predicts that the test-object will not reconstruct well if $I > 0.28$. The 5 test-objects were placed according to the locations and directions indicated in fig. 6. The positions of coronal slice $y = -23$, and transverse slices $z = 0$ and $z = 10$ are shown.

The analytic reconstructions were performed on one coronal tomographic slice ($y = -23$) and two transverse slices ($z = 0$ and $z = 10$) as indicated in fig. 8. The reconstructed slices were of size 1024 x 1024 with cubic voxels of side 0.175 mm. The reconstruction algorithm was a refined version [18] of the reconstruction code described in [15]. Briefly, the algorithm performed a rebinning to the 3D Radon domain followed by a standard reconstruction from a large Radon array as described in [15]. The rebinning step from cone-beam projections to the derivative of the 3D Radon transform was slightly different from the earlier implementation however. The parameters of the required samples of the 3D Radon array were determined by the specified reconstruction geometry. Samples which corresponded to planes passing through a vertex point were directly available from the cone-beam projection data (by applying Grangeats formula [3]). For the other samples, a nearest neighbor approach was adopted which amounted to finding the nearest available plane (containing a vertex) to the required sample plane. The nearest plane was defined as one making the smallest angle with the desired plane, and also sharing a certain point P_0. The point P_0 was specified as the point on the desired plane that was closest to the center of the field-of-view (FOV). As will be apparent for the results, this method of reconstruction was more accurate near the center of the FOV, and we adjusted the method to allow other preferred locations of reconstruction. The algorithm accepts a "focus" point F, and the nearest neighbor scheme would use the point P_0 as the closest point on the desired sample plane to the point F. We ran five additional reconstructions, with F set equal to x_i for $i = 1, 2, 3, 4, 5$.

For limited-data circumstances such as the 12 pinhole system, most iterative algorithms have the advantage over analytic techniques of blindly using all equations in the forward model to search for solutions, whereas analytic methods are rarely designed for incomplete data and there is generally no assurance that the solutions these methods provide even satisfy the imaging equations at regions of incomplete data. The disadvantage of iterative techniques is the need to model the entire object, which would be prohibitively large if the breast and five test-objects were all included with sufficiently small voxels. Therefore, for the iterative algorithms we applied, two different simulated projection data were used. The first used only object 4, and the second used only object 5. In the first case, the object distribution was replaced by a background sphere of intensity 1, centered at test-object 4, with diameter 15 mm (and object 4 was included). In the second case, only object 5 was simulated, including a 15 mm diameter background sphere of intensity 1. Both of these scenarios are equivalent to telling the reconstruction *a priori* the exact location and density of the breast and the remaining test-objects. However, the size of the reconstruction problem is now far smaller, with fewer (nonzero) data measurements and a much smaller collections of unknowns (fewer voxels to reconstruct). Similar studies with test-objects 1,2, and 3 are not shown here because the behavior was essentially the same as that of object 5.

Two iterative image reconstruction algorithms were used for these two reduced-scale datasets (isolated test-objects 4 and 5). The two algorithms were a total variation (TV) regularized least-squares (LS) method and a L_1-norm regularized LS algorithm, both with non-negativity constraints. The cost function for the TV-regularized method was of the form $(1/2)||Af - g||^2 + \lambda||\nabla f||_1$ where $||\cdot||$ is the usual Euclidean (L_2) norm and $||\cdot||_1$ is the L_1 norm. Here A is the discretized version of the forward model (equation (1)), and f and g are the discretized descriptions of the unknown function and projection data respectively. The TV regularization term, $||\nabla f||_1$, uses the L_1 norm and is the "anisotropic" form. A Landweber type algorithm was used to minimize the cost function for fixed values of λ. Our implementation was slightly adapted from the description given by Loris and Verhoeven [41]. Specifically, for fixed values of $\tau = 0.98/||A^tA||$ and $\sigma = 0.084$, the update steps were

$$f^{(n+1)} = \left(f^{(n)} + \tau A^t(g - Af^{(n)}) - \tau D^t w^{(n+1)}\right)_+ \quad (9)$$

where A^t is the backprojection operator, the transpose of A; and D is the derivative operator (a matrix with only two non-zero values in each row, +1 and -1); $(u)_+ = (u + |u|)/2$, understanding that for a vector argument, each component of the vector which is negative is assigned to zero; and where

$$w^{(n+1)} = P_\lambda(w^{(n)} + (\sigma/\tau)Dk^{(n+1)}) \quad (10)$$

$$k^{(n+1)} = f^{(n)} + \tau A^t(g - Af^{(n)}) - \tau D^t w^n \quad (11)$$

with

$$P_\lambda(u) = \begin{cases} \lambda\,\mathrm{sgn}(u) & |u| > \lambda \\ u & |u| \le \lambda \end{cases} \quad (12)$$

understanding that when P_λ is applied to a vector, the above formula is applied separately to each component of the vector. The iterations were initialized with $f^{(0)} = 0$ and $w^{(0)} = 0$. We note that for $\lambda = 0$ the iterations simplify to $f^{(n+1)} = (f^{(n)} + \tau A^t(g - Af^{(n)}))_+$ which is a Landweber update that converges to a minimizer of the data-fidelity term within the set of non-negative solutions. Larger values of λ increase the weight of the TV constraint.

This article has been accepted for publication in a future issue of this journal, but has not been fully edited. Content may change prior to final publication. Citation information: DOI 10.1109/TRPMS.2019.2918222, IEEE Transactions on Radiation and Plasma Medical Sciences

The cost function for the L_1-norm regularized method is $||Af - g||^2 + \lambda||f||_1$ with the constraint $f(x) \geq 0$. The algorithm also used a Landweber type iteration, but with soft-thresholding [42]. Our implementation used the following update steps:

$$f^{(n+1)} = S_{\lambda\tau/2}\left(f^{(n)} + \tau A^t(g - Af^{(n)})\right) \tag{13}$$

where $\tau = 0.98/||A^tA||$ and

$$S_\lambda(u) = \begin{cases} u - \lambda & u > \lambda \\ 0 & u \leq \lambda \end{cases} \tag{14}$$

which is applied component-wise when the argument to S_λ is a vector. The algorithm was initialized with $f^{(0)} = 0$. When $\lambda = 0$ the algorithm simplifies to the same non-negative Landweber update $f^{(n+1)} = (f^{(n)} + \tau A^t(g - Af^{(n)}))_+$.

Although the implementation of our L_1-norm constraint algorithm is different from that described by Li et al [43], the method is very much in the same spirit. The idea is that by applying a $||f||_1$ penalty, reconstructed images with more zeros are preferred by the algorithm. We also applied the L_1-norm algorithm to the same two data sets (test-objects 4 and 5) but with the 10% background spheres removed, to allow this L_1 sparsity preference to manifest itself more strongly. The gaps between the disks should now preferentially reconstruct to zero, rather than to the small positive background.

V. Results

A. Circular vertex trajectory

Figure 9 shows a central slice through each of the three reconstructed test objects. For the test-object located at $z = 10$ mm, the disks have been cleanly reconstructed with little signs of artifacts, which is consistent with the calculated value $I(x_1, \theta_z)$ = 0.10. The intensity profile, plotted along the axis of the test-object shows clear separation of the disks. In the image, some negative undershoots appear at the edges of the disks, and these are a known characteristic of reconstructed disk phantoms in circular CB tomography. For the second test phantom, at $z = 29$ mm, the disks have bulged out at the center in their reconstructed images and are now virtually touching each other. The visual interpretation is more favorable than the intensity values plotted along the axis of the test object where it is very difficult to discern the separation of the three

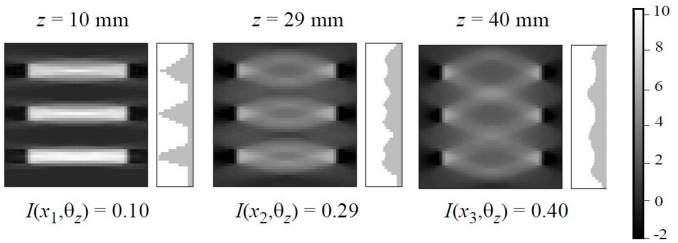

Fig. 9. FDK reconstructed images from the circle of 60 vertices. A vertical slice is shown passing through the center of each test-object. On the right of each image is a profile plot of the intensities along the central vertical line through the objects (along the z-axis). Left: test-object centered at z = 10 mm. Middle: test-object at $z = 29$ mm. Right: test-object at $z = 40$ mm.

disks. These observations are in agreement with the predicted behavior based on the calculated incompleteness value of $I(x_2, \theta_z)$ = 0.29. Finally, for the third test object, centred at $z = 40$ mm, the reconstructed disks have now distorted so much that there is dramatic cross-talk and overlapping of the features. With a minimum incompleteless level of $I(x_3, \theta_z) = 0.40$, the standard disks phantom could not be perfectly tomographically separated. Both visually and using the plotted profile, it is not possible to reliably separate these three disks along the axis of the phantom. We note that the edges of the disks are still separated, which can give some visual impression of resolving the test-object. The central vertical profiles shown to the right of the images provide a less subjective interpretation of separation of the disks. Recall however, that the separation criterion applies along the central axis of the test object.

In fig. 10, the reconstructions of the three new test-objects are shown. At x_3 ($z = 40$ mm), the test object threshold is 0.57 which is larger than the incompleteness value $I(x_3, \theta_z)$ = 0.40 so no prediction of blurring the disks can be made. Indeed, the reconstructed disks are distorted but still clearly separated. At x_2 ($z = 29$ mm) the test object threshold is 0.20 whereas $I(x_2, \theta_z) = 0.29$ so according to our theory, the disks cannot be tomographically separated (along the phantom axis) which is in agreement with the observed reconstruction (fig. 10), middle row, right). Lastly, at x_1 ($z = 10$ mm) this test-object threshold is 0.083 whereas the calculated incompleteness value is 0.10, so the disks will not be completely tomographically separated. The bottom right image of fig. 10 confirms that the disks are not cleanly separated along the central axis. The intensity profiles do not drop to zero. The bottom two disks are nearly separated, whereas the top two are more blurred. This effect is because at this location, the incompleteness value at the space between the top two disks is 0.11 and between the bottom two disks it is 0.09. The incompleteness value for the bottom two disks is only slightly larger than the test-object threshold of 0.083.

In fig. 11 (left), the reconstruction of the standard test-object centred at x_1 is shown, from substantially truncated projections; it corresponds to the fig. 9 (left) where the same object was reconstructed from non-truncated projections. With the truncated projections, streak artifacts from the dense object passed through the center of the test object making it impossible to separate the disks at that location. The example was carefully chosen, and is obviously an extreme case, but it illustrates that point that the $I(x, \theta)$ metric indicates a *minimal* level of incompleteness.

The results of these numerical experiments are in complete agreement with the proposition that the incompleteness value $I(x, \theta)$ can quantitatively predict at what point the disks will fail to be separated along their axis. The incompleteness value is a "minimum" level of incompleteness, so in some situations, the disks might fail to be separated even if $I(x, \theta)$ is lower than the test-object threshold. However, for the examples shown which did not involve projection truncation, the results matched the predictions exactly. Note that the metric is not designed to specifically predict the reconstruction outcome of the test-objects; the purpose of the test-objects is to illustrate

This article has been accepted for publication in a future issue of this journal, but has not been fully edited. Content may change prior to final publication. Citation information: DOI 10.1109/TRPMS.2019.2918222, IEEE Transactions on Radiation and Plasma Medical Sciences

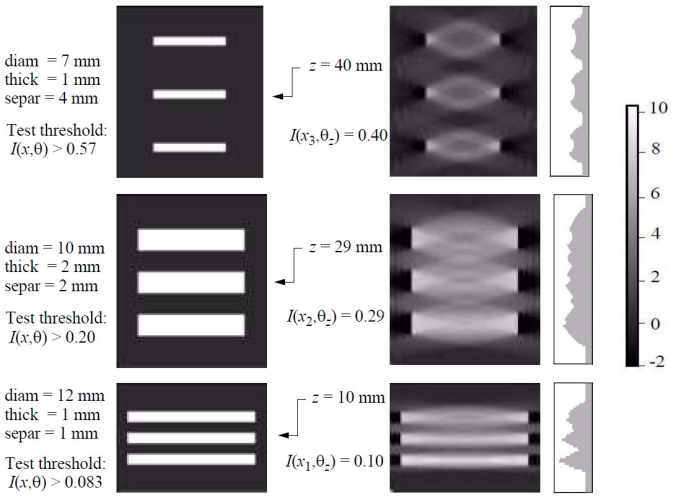

Fig. 10. Left column: three new disk phantoms, with diameter, thickness, and separation shown. Our incompleteness theory states that for the top phantom, the axis will not be tomographically separated if $I(x,\theta) > 0.57$; the middle phantom for $I(x,\theta) > 0.2$; the bottom phantom, for $I(x,\theta) > 0.083$. Right column: FDK reconstructed images of the three new disk phantoms placed at the same locations in the same geometry as shown in fig. 9. At the right of each image is an intensity profile taken along the central vertical line through the disks. Top row: disks positioned at $z = 40$ mm, where $I = 0.40$. Middle row: disks positioned at $z = 29$ mm, where $I = 0.29$. Bottom row: disks positioned at $z = 10$ mm, where $I = 0.10$.

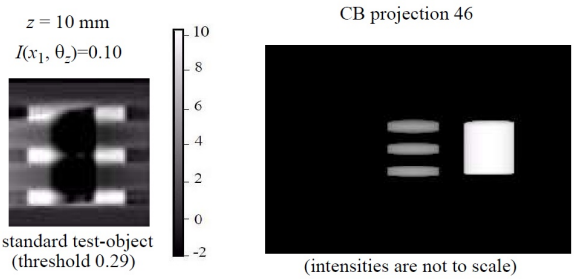

Fig. 11. Reconstruction of standard test-object from truncated projections. A dense cylinder was centered at height 20 mm, and at nearly 55 mm from the center of the transverse plane. Right: one of the 20 non-truncated projections showing the dense cylinder "behind and to the right" of the disks test-object. Left: FDK reconstruction of the test-object showing a negative streak artifact from the cylinder crossing directly through the axis of the disks.

failure of tomographic recovery when the incompleteness metric exceeds the test-object threshold.

Central coronal reconstructions of the shell+bubble phantom in its two locations are shown in fig. 12. It is immediately obvious that the reconstructions of the phantom in the region of the bubble differ, with the bubble appearing in the interior of the phantom in the first case, and inside the shell in the second case. These images illustrate that the same object can be reconstructed differently when placed in different locations, and when there are large incompleteness values at play. In this case, with $I(x_1,\theta) = 0.53$ for the position of the bubble in the first image, the reconstruction must be considered less reliable at that location. In the second image, with the bubble located at x_2, the incompleteness value is $I(x_2,\theta) = 0.037$ so the degree of image artifact is likely to be much lower. We note in particular that no blatantly obvious feature of the images indicate the presence of artifacts (no obvious streaks or blurring).

B. 12 pinhole vertices

The second row of fig. 13 shows the three reconstructed slices from the 12 simulated pinhole projections. Although the main concern is the reconstruction of the 5 test-objects, we note that the overall shape of breast is reasonably well recovered, with many of the streaks and artifacts probably related to the presence of the small high-intensity disks.

The two test-objects lying inside the Tuy region, objects 1 and 5, were reconstructed satisfactorily, with clear visual separation of the three disks. Test-object 4 was recovered poorly with little suggestion that three disks were present at that location. These results might have been anticipated using only standard reconstruction theory, with some assumption that the sampling of the rectangular curve was sufficient for the frequency information sought in the test-objects. Conventional theory would probably not have predicted the outcome of test-object 2, where the disks were also well separated in agreement with our model (which did not predict serious artifacts in that orientation at that location). However, test-object 3 was very poorly recovered, although our model suggested comparable or better behavior than objects 2 and 5.

This poor recovery of test-object 3 does not contradict the predictions of our model, which is only strong enough to say that the disks of test-object 4 will not be resolved, and does not ensure that the other objects can be resolved. However, the geometry did not suggest that test-object 3 was unfavorably located or oriented. In this case, it turned out that the reconstruction algorithm was not providing the best possible results at location 3. We were aware that the reconstruction algorithm favored the center of the FOV, so we ran a modified version as outlined in Sec. IV-B, setting $F = x_3$. The images obtained from this version of the algorithm are shown in the third row of fig. 13. Small changes appeared in almost all features of the reconstruction, including

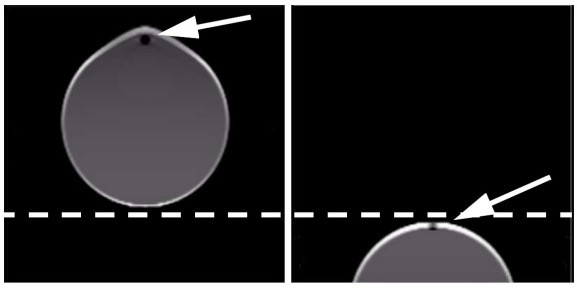

Fig. 12. A central slice, containing the z-axis, of the shell+bubble phantom reconstructed using the FDK algorithm from 60 CB projections along a circular trajectory. The dotted white line indicates the level of the $z = 0$ plane in which the 60 CB vertices lie. Left: the phantom was positioned 100 mm above the $z = 0$ plane. The arrow indicates the location of x_1 where $I(x_1, theta_z) = 0.53$. Right: the phantom was positioned 100 mm below the $z = 0$ plane. The arrow indicates x_2 with $I(x_2,\theta_z) = 0.037$. The position of the bubble with respect to the shell is different in the two reconstructed images.

This article has been accepted for publication in a future issue of this journal, but has not been fully edited. Content may change prior to final publication. Citation information: DOI 10.1109/TRPMS.2019.2918222, IEEE Transactions on Radiation and Plasma Medical Sciences

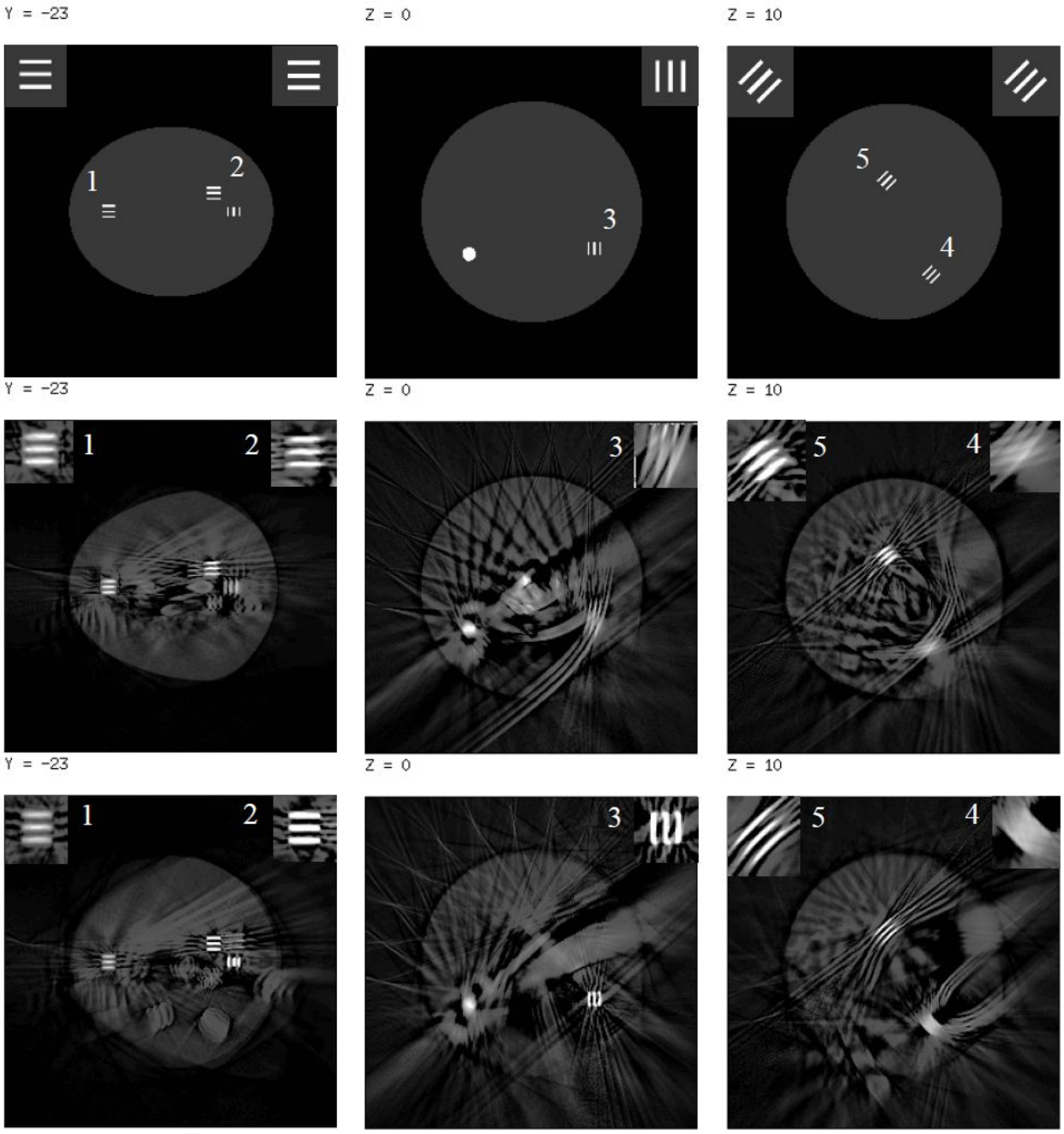

Fig. 13. Reconstruction images from the 12 pinhole geometry. Column 1: coronal slice $y = -23$. Column 2: transverse slice $z = 0$. Column 3: transverse slice $z = 10$. (See fig. 8 for visualization of the slice locations.) Top row: slices through the simulated phantom. Middle row: reconstructions from simulated data using the algorithm of [15]. Bottom row: reconstructions using a modified algorithm which treats x_3 (location of test-object 3) as the focus point of the algorithm (see text). These simulation results originally appeared in a [19] in a slightly different context.

the degree of recovery of the test objects. In this case test-object 3 was well resolved. Consistent with the predictions of the model, test-object 4 was still not resolved.

The position of test-object 4 and the action of the particular reconstruction algorithm could explain the poor reconstruction (fig. 13, bottom right) at that location. Figure 14 shows the results of 5 different reconstructions, corresponding to $F = x_i$ for $i = 1, 2 \ldots, 5$. Only the reconstruction details of the relevant test-object are displayed (for $F = x_i$, only the ith test object is displayed with a coronal and transverse slice through the center of the disks). Here it is immediately apparent that the individual disks of test-objects 1, 2, 3, and 5 are clearly resolved, and test-object 4 remains heavily blurred with only faint suggestions of three disks. In this reconstruction, the edges of object 4 do appear to be resolved, similar to the behavior observed for the circular study in fig. 9 (right) which corresponded to the same incompleteness value of $I(x, \theta) = 0.4$.

For the TV regularized and L_1 regularized reconstructions of the isolated test objects 4 and 5, we used 500 Landweber

This article has been accepted for publication in a future issue of this journal, but has not been fully edited. Content may change prior to final publication. Citation information: DOI 10.1109/TRPMS.2019.2918222, IEEE Transactions on Radiation and Plasma Medical Sciences

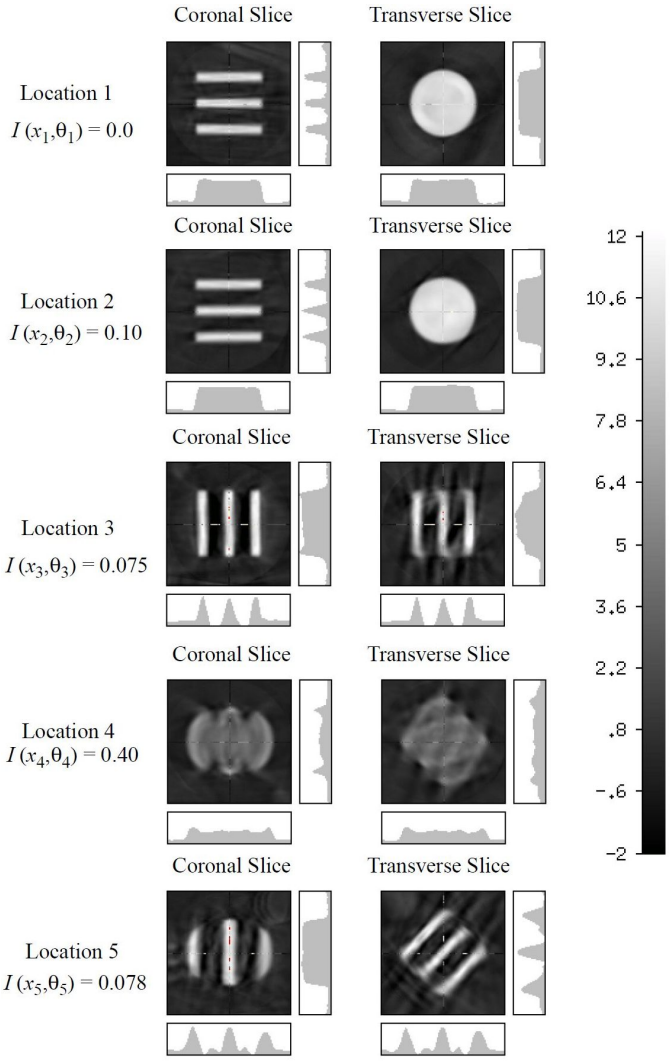

Fig. 14. Results of 5 versions of the analytic reconstruction algorithm, each applied by assigning F to the center of a test-object. The transverse slice at location 3 is the same reconstruction shown in the third row of fig. 11. Consistent with the predictions of the model, test-object 4 is not resolved. (Faint cross-hair lines are visible in some images, showing the location of the central horizontal and vertical profiles displayed adjacent to the images. The two horizontal profile lines are parallel and very close to each other in the 3D geometry.)

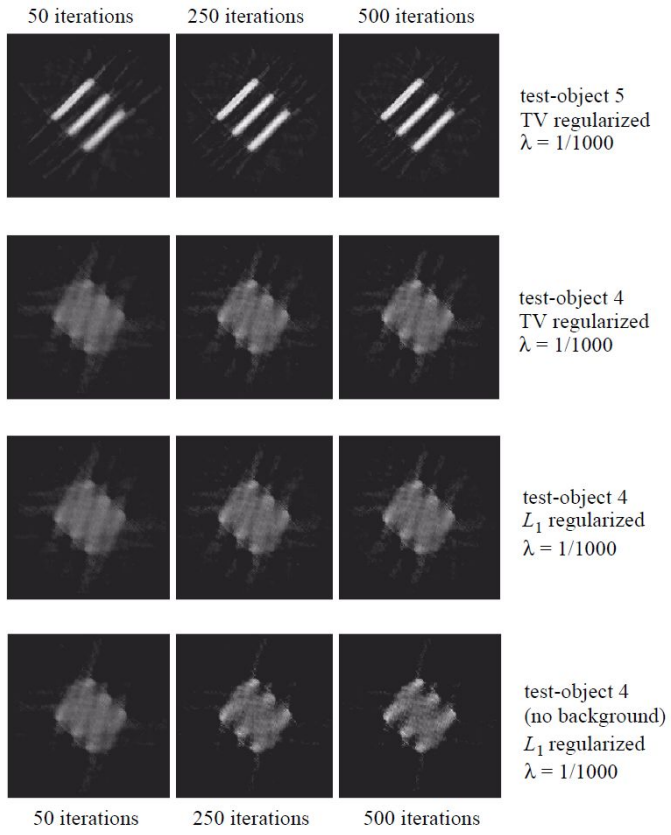

Fig. 15. Convergence of the iterative algorithms - various examples of transverse reconstructed slices from 12 CB projections, of the isolated test-objects. Left column: 50 iterations, middle: 250 iterations; right 500 iterations. For both the TV and L_1 regularized reconstructions, using either test-object 4 or test-object 5, with or without background, essentially no visible change is observable between 250 and 500 iterations.

iterations for all reconstructions, which we justified by observing only miniscule visible changes between 250 iterations and 500 iterations. The images of fig. 15 shows the progression for a selection of the experimental studies.

Both of the iterative algorithms depend on a fixed regularization parameter λ. We performed reconstructions for $\lambda = 10^{-7}, 10^{-6}, \ldots, 1$. Visually, the images obtained for all λ values below $\lambda = 10^{-3}$ were very similar. The pixel intensities changed in the second decimal place when λ decreased from 10^{-3} to 10^{-4}, and only in the third decimal place when decreased from there down to 10^{-7}. We present the reconstruction images for $\lambda = 1$ and $\lambda = 10^{-3}$ only.

Transverse and coronal slices through the TV-regularized reconstructed images of test-objects 4 and 5 are shown in fig. 16. We observe very similar results to the analytic reconstructions of fig. 14. Even though the iterative reconstructions were performed with the objects isolated (rather than all present simultaneously, including the background from the right breast) we found that reconstructed test-object 4 seemed to be equally blurry and was visually similar to the analytic reconstructions, and test-object 5 was cleanly reconstructed, as before. Increasing the TV-penalty (i.e. increasing the λ parameter) visually improved the reconstruction of test-object 5, but did not help separate the disks of reconstructed test-object 4, especially near the central axis.

Reconstructed images from the L_1-regularized algorithm are shown in fig. 17. As before, only central transverse and coronal slices are presented. We immediately observe that in all cases, test-object 5 was cleanly reconstructed, with clear separation of the disks, just as when the TV algorithm (fig. 16) and the analytic algorithm (fig. 14) were used. For test-object 4, we note visually comparable reconstructions at $\lambda = 10^{-3}$ to those of the TV and analytic algorithms. When increasing the L_1-norm penalty ($\lambda = 1$), a discernible improvement is visible in the reconstructed images. For the case where the 10% background was removed from the data, a more pronounced improvement can be seen (bottom row of fig. 17), suggesting that the non-negativity constraint had at least as much influence as the L_1 penalty. In all cases, however, the gap between the disks of test-object 4 was not visible along the

This article has been accepted for publication in a future issue of this journal, but has not been fully edited. Content may change prior to final publication. Citation information: DOI 10.1109/TRPMS.2019.2918222, IEEE Transactions on Radiation and Plasma Medical Sciences

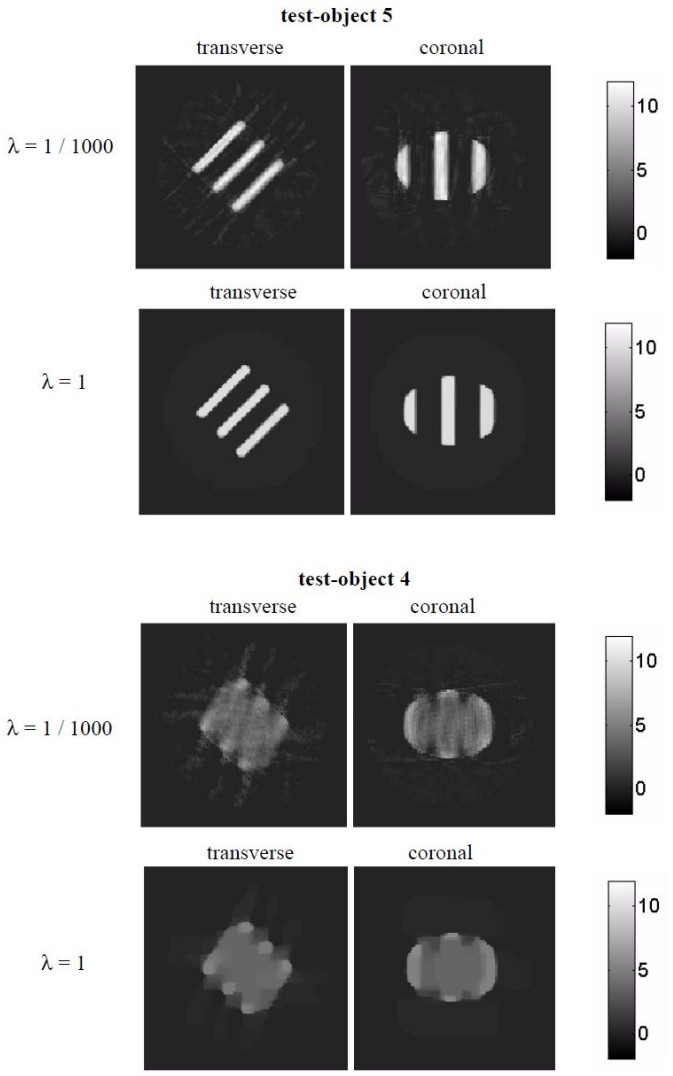

Fig. 16. Total variation (TV) regularized reconstructions of test-object 4 (below) and test-object 5 (above). The value of λ indicates the weight applied to the TV regularization term (see text). The 15 mm diameter background sphere (intensity 1.0) is faintly visible in the second row (test-object 5, $\lambda = 1$). These images, from isolated test-object simulations, are to be compared with those of fig. 12, rows 4 and 5. As predicted, the disks of test-object 4 are not separated in the reconstructed images.

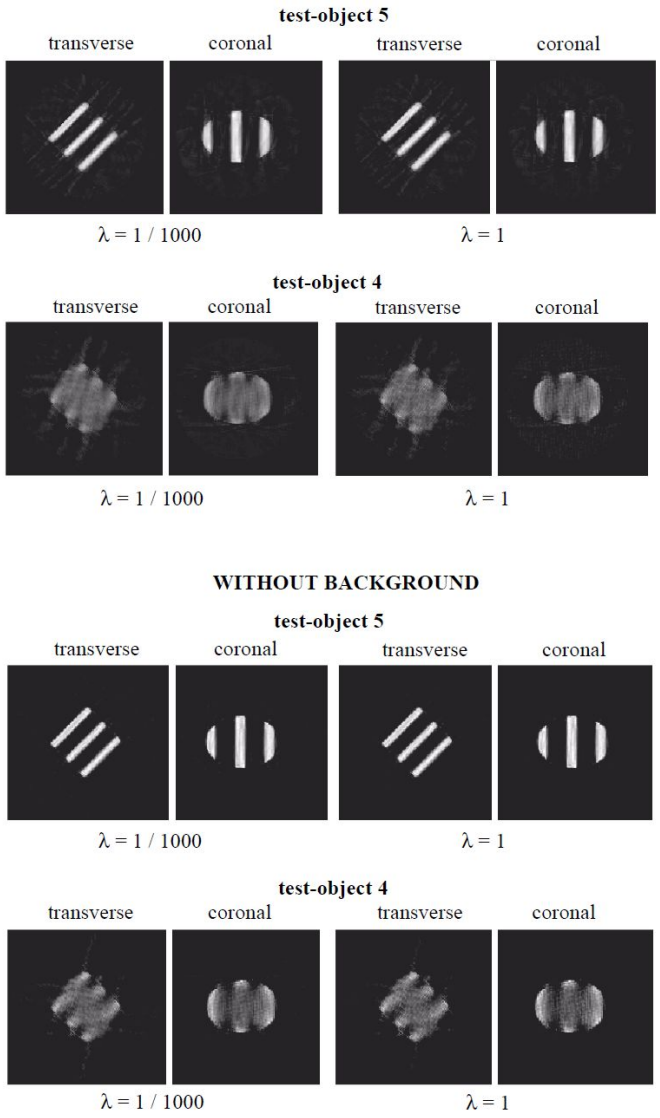

Fig. 17. L_1-norm regularized reconstructions of isolated test objects 4 and 5. Top two rows: with the 10% background sphere. Bottom two rows: without the background sphere. Only miniscule visible differences appear when adjusting the regularization weight (λ). Some improvement appears in the reconstruction of test-object 4 when no background sphere is present, and the non-negativity constraint has more effect. Nevertheless, the central axis of the 3 disks remains blurred.

central axis of the phantom, as predicted by the incompleteness metric.

VI. Discussion and conclusions

For cone-beam tomography, we have defined a tomographic incompleteness metric $I(x, \theta)$ that is based on known sufficiency conditions for data incompleteness [2]. These conditions are local and depend only on the geometry of the cone vertices with respect to the location under scrutiny. The detector is assumed to have perfect spatial resolution so it plays no role in the definition of $I(x, \theta)$ unless the measurement line from the vertex to is truncated (misses the detector), in which case the vertex is excluded when considering the location x. The incompleteness metric is independent of the object being scanned, and independent of the image reconstruction algorithm applied. A positive value for our data incompleteness function indicates the (minimal) level of incompleteness that exists at the particular location, and in a particular direction θ.

Using small test-objects we have given concrete demonstrations of the effects of data incompleteness in tomographic reconstruction, and our examples support our claim that these effects are independent of the image reconstruction algorithm applied. If the calculated incompleteness value at x in direction θ is $I(x, \theta) = k$ then a small disk phantom made of parallel disks of unit diameter will be difficult to tomographically resolve along its axis if their separation is less than k units, (where the disks are oriented perpendicularly to θ, and centred at x). Our results demonstrated this behavior over two very different imaging geometries, and using several different analytic and iterative reconstruction algorithms.

This article has been accepted for publication in a future issue of this journal, but has not been fully edited. Content may change prior to final publication. Citation information: DOI 10.1109/TRPMS.2019.2918222, IEEE Transactions on Radiation and Plasma Medical Sciences

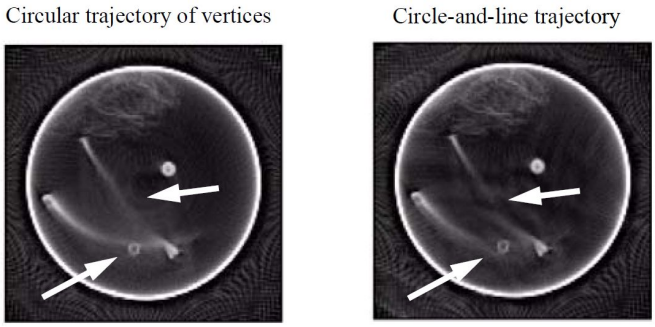

Fig. 18. The same transverse slice of a reconstructed storage drum from real data taken on a circular vertex trajectory (left) and a circle-and-line vertex trajectory (right). The incompleteness values (in the axial direction) were much higher for the circular vertex trajectory in this slice. For the circle-and-line trajectory, all incompleteness values were low. (Images were taken from [44]; see also [45] and [16] for more information.) See text for explanation of the features indicated by the white arrows.

Because the metric is only based on sufficiency conditions, a value of $I(x,\theta) = 0$, meaning "no incompleteness," is not an assertion of local data *completeness*. Sufficient conditions for data completeness at a given location are much more complicated and depend on the support of the object being scanned relative to the cone vertices, as well as the incompleteness values elsewhere in the object. Furthermore, completely general necessary and sufficient conditions for tomographic completeness in CB tomography are not yet known.

We emphasize that incompleteness at various (x,θ) of a CB geometry does not imply that artifacts are inevitable for all objects and all reconstruction algorithms. It only means that certain features will be very difficult to reconstruct. In particular we were not able to accurately reconstruct the features of the small disk phantoms. In general, the features in question are likely to be surfaces normal to the direction θ, but the specific artifacts manifested are liable to depend on the reconstruction algorithm (how the algorithm handles incomplete data). For our test objects, a blurring appeared between the disks, but less obvious artifacts can occur as evidenced by the behavior on the shell+bubble phantom (fig. 12). A similar but less dramatic effect of incompleteness in circular CB with real data was observed with an industrial scan of the contents of a storage drum. In fig. 18 (left) the lower curved structure appears to actually intersect with a small disk like object (see bottom arrow) and also with the second, straighter structure. This second structure appears as a single piece. A second scan taken with additional CB projections (a tomographically complete "circle-and-line" trajectory) revealed that the second structure was really two pieces, and the first structure was shorter than appeared in the previous reconstruction. In motion-corrected helical CT, incompleteness artifacts presented in [31] primarily consisted of streaks with some blurring of local features. Incompleteness artifacts can be innocuous, so a calculation of $I(x,\theta)$ throughout the imaging region is recommended, to anticipate where incompleteness artifacts are likely to occur.

The formula for our incompleteness metric $I(x,\theta)$ is similar to other metrics that have been suggested for CB data completeness and incompleteness. We can informally describe $I(x,\theta)$ as "$\min|\tan\psi_i|$" where ψ_i is the angle made by the ray from x to vertex a_i with respect to the plane passing through x with normal θ. A popular alternative choice is to take the fraction of all directions θ such that $I(x,\theta) = 0$ as a heuristic completeness measure at the point x [23], [26], [27], [28], [29]. It was pointed out in [28] that this metric provided a *necessary* completeness condition (which is equivalent to saying the metric provides a sufficient incompleteness condition). Other variations include averaging $|\cos\psi_i|$ over all (so a value of 1 at location x indicates data completeness) [24], and taking the maximum value of$|\sin\psi_i|$ over all θ as an incompleteness metric [31]. The metric we propose here has been previously described in conference proceedings papers [18], [17], [19], [46] but as a heuristic approach to defining resolution in tomographic reconstructions. (Although incompleteness causes a blurring of the test-object features, we prefer to call this "poor tomographic recovery" rather than "poor resolution", because the effect scales with the size of the object which is not the usual meaning of "resolution.") These are the only cases where the stratification according to θ was maintained, whereas other metrics use an average or maximum value to compress the θ variable. The advantage of this stratification is that $I(x,\theta)$ provides a quantitative description of the (best-case) behavior of the reconstructed test-objects, thereby providing concrete verifiable examples of what can go wrong when $I(x,\theta) \neq 0$, as our simulations studies have demonstrated. For example, test-objects 2,3, and 4 in the breast phantom simulation were in roughly the same location with similar patterns of measured lines, as can be seen from the polar plots of fig. 7. Any metric that condenses the angular information would assign very similar values to these three positions. However, we have demonstrated that the test-object will behave very differently depending on its orientation, with test-object 4 having a particularly unfavorable orientation.

A potential weakness of the $I(x,\theta)$ definition is that the value is determined by the location of a single "best" CB vertex with angle $\psi_{\min}$. It could be supposed that the positions of remaining vertices would also affect location incompleteness. For example, at some location x, if all the vertices provided the same value of $\psi_{\min}$ $(= \min|\tan\psi_i|)$, then "better reconstruction" might be expected than if the remaining vertices all had much larger values $\psi_i > \psi_{\min}$. However, our experimental simulation show this not to be the case, and provides a justification for the simple "one best vertex" approach to defining $I(x,\theta)$. For the first simulation geometry with 60 vertices on a circle, at the location 40 mm above the centre of the circle (fig. 4), we obtained $I(x,\theta_z)$ = 0.40. In this case, all 60 vertices had the same minimal angle $\psi_{\min}$. In the second simulation, position 4 also had $I(x,\theta)$ = 0.40, but this value was determined by only one of the 12 vertices, the other vertices giving larger values of ψ_i (see fig. 7, where the 12 dark bands are different distances from the white "+"). However, the reconstructed images of the test object consistently had the same visual quality, when comparing fig. 9 (right) with fig. 14, or with the various reconstructions of fig. 16 or fig. 17. This result strongly supports the proposed definition for $I(x,\theta)$ that uses the single best CB vertex, irrespective of the distribution

This article has been accepted for publication in a future issue of this journal, but has not been fully edited. Content may change prior to final publication. Citation information: DOI 10.1109/TRPMS.2019.2918222, IEEE Transactions on Radiation and Plasma Medical Sciences

of the remaining vertices.

We have noted that test-object 4 of the breast study was reconstructed with similar blurring behavior to the test-object at $z = 40$ mm for the circular study; in both cases, $I(x, \theta) = 0.40$. We also note that the reconstructions of test-objects 2 and 3 in the breast simulations study (fig. 14 left, rows 2 and 3) showed a similar slight blurring along the axis as that of fig. 9 (left) for the circular study. This blurring is more quantitatively evident in the axial profile plots shown next to the images. The incompleteness values were 0.10, 0.075 for the breast study and 0.10 for the circular study with very different geometric contributions of the CB projections. The agreement of the reconstructed images with the incompleteness values also supports the quantitative nature of the definition of $I(x, \theta)$, and its universal applicability.

When considering a test-object at x of unit-diameter disks separated by k units, we are claiming that if the incompleteness value $I(x, \theta)$ is greater than k then it will be very difficult to tomographically resolve the test-object along its axis. The reason is that $I(x, \theta) > k$ implies that any measurement line passing through the axis will be inclined by more than the angle $\tan^{-1} k$ with respect to the central plane parallel to the disks, and therefore will pass through both disks. Therefore, no measurement lines exist that pass between the disks and intersect the axis of the phantom. On the other hand, it is geometrically possible for steeper lines to pass between the disks if they do not pass through the central axis, thus allowing the outer edges of the test-object to be resolved. For our test object of diameter 7 mm and separation 2 mm, we have $k = 2/7$. However, at 2.5 mm from the axis of the test-object (1 mm from the edge) the "equivalent" value would be $2/(2\sqrt{3.5^2 - 2.5^2})$=$1/\sqrt{6} \approx 0.41$, so incompleteness values of $I(x, \theta) = 0.40$ would be compatible with resolving the outer 1 mm edge of the disks. In figs. 9, 14, 16, 17, the edges of the test-object (located and oriented such that $I(x, \theta) = 0.40$) were visibly resolved.

This feature of the disks phantom, of non-uniform response to incompleteness when moving away from the central axis, is a disadvantage of this choice of test-object. One possible way to avoid this non-uniform response would be to use concentric spherical shells as was applied in [31]. This concentric-shells phantom has the additional advantage of simultaneously responding to all directions θ. However, it would be less obvious to identify how the spacing of the shells would relate quantitatively to incompleteness values. Furthermore, for physical experiments, phantoms made of small disks, possibly with an adjustable spacing, would be much easier to fabricate for x-ray and SPECT studies.

In summary, we propose a measure of local directional incompleteness in CB tomography. The incompleteness model is easily applied because the metric is geometric, based only on the location of the CB vertices, and assumes ideal CB projections (no physical effects such as photon counting statistics, Compton scatter effects) with perfect detector resolution. No assumptions are made on the physical extent ("support") of the object being scanned. Our model describes tomographic incompleteness both inside and outside the convex hull of the CB vertices. We have used computer simulations with test phantoms to quantitatively verify the effects of incompleteness on reconstructed images. We used two different analytic reconstruction algorithms and two different iterative algorithms in our studies. Further verification of this incompleteness model could include studies with complex patterns of truncated projections, and experimental studies with real data.

ACKNOWLEDGMENT

We thank Dr. Simon Rit of CREATIS Laboratory (Lyon, France) for providing a packaged version of the FDK reconstruction algorithm from the Reconstruction Tool Kit (RTK).

REFERENCES

[1] H. K. Tuy, "An inversion formula for cone-beam reconstruction" *SIAM J. Appl. Math*. vol 43, pp.546-552, 1983.

[2] D. Finch, "Cone-beam reconstruction with sources on a curve" *SIAM J. Appl. Math.* vol 45, pp. 665-673, 1985.

[3] P. Grangeat, "Mathematical framework of cone-beam 3D reconstruction via the first derivative of the Radon transform" in Mathematical methods in tomography, G. Herman, A. Louis F. Natterer eds., Lecture Notes in Mathematics 1497, Springer-Verlag, Berlin. pp. 66- 97, 1991.

[4] A. Katsevich, "Theoretically exact filtered backprojection-type inversion algorithm for spiral CT" *SIAM J. Appl. Math*. vol. 62, pp.2012-2026, 2002.

[5] Y. Zou, X. Pan, "Exact image reconstruction on PI-lines from minimum data in helical cone-beam CT" *Phys. Med. Biol*. vol 49, pp. 941-959, 2004.

[6] J. D. Pack, F. Noo, R. Clackdoyle, "Cone-beam reconstruction using the backprojection of locally filtered projections" *IEEE Trans. Med. Imag.* vol. 24, pp 70-85, 2005.

[7] H. Kudo, T. Saito, "Derivation and implementation of a cone-beam reconstruction algorithm for nonplanar orbits" *IEEE Trans. Med. Imag*. vol 13, pp.196-211, 1994.

[8] M. Defrise, R. Clack "A cone-beam reconstruction algorithm using shift-variant filtering and cone-beam backprojection" *IEEE Trans. Med. Imag.* vol. 13, pp.186-195, 1994.

[9] R. Clackdoyle, F. Noo, F. Momey, L. Desbat, S. Rit, "Accurate transaxial region-of-interest reconstruction in helical CT?" *IEEE Trans. Rad. Plasma Med. Sci.* 1:346-357, 2017.

[10] H. H. Barrett, H. C. Gifford "Cone-beam tomography with discrete data sets" *Phys. Med. Biol.* vol. 39, pp. 451-476, 1994.

[11] E. T. Quinto, "Singularities of the x-ray transform and limited data tomography in $\mathbb{R}^2$ and $\mathbb{R}^3$," *SIAM J. Math. Anal*. vol. 24, pp. 1215-1225, 1993.

[12] P. A. Rattey, A. G. Lindgren, "Sampling the 2-D Radon transform" *IEEE Trans. ASSP* vol. 29, pp. 994-1002, 1981.

[13] F. Natterer, "Sampling in fan-beam tomography" *SIAM J. Appl. Math.* vol. 53, pp. 358-380, 1993.

[14] L. Desbat, "Echantillonage parallle efficace en tomographie 3D" *C.R. Acad. Sci. Paris*, vol. 324(I), pp.1193-1199, 1997.

[15] F. Noo, R. Clack, M. Defrise, "Cone-beam reconstruction from general discrete vertex sets using Radon rebinning algorithms" *IEEE Trans. Nuc. Sci*. vol. 44, pp. 1309-1316, 1997.

[16] R. Clackdoyle, M. Defrise, F. Noo "Early results on general vertex sets and truncated projections in cone-beam tomography" IMA Volumes in Mathematics and Its Applications Volume 110. Computational Radiology and Imaging: Therapy and Diagnostics. C.Borgers, F.Natterer (Eds.) Springer, New York, pp. 113-135, 1999.

[17] F. Noo, R. Clackdoyle, "Sampling strategies and resolution in limited data cone-beam tomography" Proceedings of the International Conference on Acoustics, Speech, and Signal Processing 2001 (ICASSP 2001). Salt Lake City, UT. IEEE Service Center, vol 3, pp. 2025 - 2028, 2001.

[18] R. Clackdoyle, F. Noo "Cone-beam tomography from limited vertex sets: theory and an algorithm" in Proceedings of the 2001 International Conference on Sampling Theory and Applications (SAMPTA 2001) May 13-17, 2001, Orlando, FL. A.I.Zayed (Ed). IEEE Operations Center Piscataway, pp. 205-212, 2001.

[19] R. Clackdoyle, F. Noo "Cone-beam tomography from 12 pinhole vertices" in Conference Record of the 2001 IEEE Nuclear Science Symposium and Medical Imaging Conference, November 4-10, 2001, San Diego. pp 1874-1876, 2002.

[20] F. Natterer, "The Mathematics of Computerized Tomography" 1986: Wiley-Teubner

[21] S. S. Orlov, "Theory of three-dimensional reconstruction. I. Conditions for a complete set of projections" *Sov. Phys. Crystallogr*. vol 20, pp. 312-314, 1975.

[22] S.D. Metzler, J.E. Bowsher, R.J. Jaszczak, "Geometrical similarities of the Orlov and Tuy sampling criteria and a numerical algorithm for assessing sampling completeness" *IEEE Trans. Nucl. Sci.* vol. 50, pp.1550-1555, 2003.

[23] S.D. Metzler, K.L. Greer, R.J. Jaszczak, "Helical pinhole SPECT for small-animal imaging: a method for addressing sampling completeness" *IEEE Trans. Nucl. Sci.* vol. 50, pp.1575-1583, 2003.

[24] F. Stopp, C. Winne, E. Jank, E. Keeve, "Quality evaluation for image recording strategies for limited angle tomography" Tsinghua Science and Technology. vol. 15, pp.25-29, 2010

[25] J. Lin, S.R. Meikle, "Truncated pinhole SPECT: sufficient sampling criteria and applications" Conference Record of the 2010 IEEE Nuclear Science Symposium and Medical Imaging Conference (Knoxville, TN. November 2010). pp.2066-2070, 2010.

[26] J. Lin, S.R. Meikle, "SPECT using asymmetric pinholes with truncated projections" *Phys. Med. Biol*. vol 56, pp 4103-4118, 2011.

[27] T. Dai, T. Ma, Q. Wei, S. Wang, H. Liu, J. Cui, Q. Huang, Y. Liu "Design and sampling completeness evaluation of scanning orbits in multi-pinhole small animal SPECT imaging" Conference Record of the 2011 Nuclear Science Symposium and Medical Imaging Conference (Valencia, Spain, November 2011). pp.2836-2839, 2011.

[28] B. Liu, J. Bennett, G. Wang, B. De Man, K. Zeng, Z. Yin, P. Fitzgerald, H. Yu, "Completeness map evaluation demonstrated with candidate next-generation cardiac CT architectures" *Med. Phys.* vol. 39, pp.2405-2416, 2012.

[29] K. Van Audenhaege, C. Vanhove, S. Vandenberghe, R. Van Holen, "The evaluation of data completeness and image quality in mutliplexing multi-pinhole SPECT" *IEEE Trans. Med. Imag.* vol. 34, pp. 474-486, 2015.

[30] R. Clackdoyle "Fully 3D Reconstrution Theory in Perspective" in Conference Proceedings of The 8th International Meeting on Fully Three-Dimensional Image Reconstruction in Radiology and Nuclear Medicine, 3D 05, Salt Lake City, Utah, July 6-9, 2005. F.Noo, L.Zeng, H.Kudo (eds), pp. 64-69, 2005.

[31] T. Sun, R. Clackdoyle, J.-H. Kim, R. Fulton, J. Nuyts, "Estimation of local data-insufficiency in motion-corrected helical CT" *IEEE Trans. Rad. Plasma Med. Sci.* 1:346-357, 2017.

[32] J. Chen, "A theoretical framework of regional cone-beam tomography" *IEEE Trans. Med. Imag.* vol. 11(3), pp. 342-350, 1992.

[33] R.Leahy, R.Clackdoyle, F.Noo, "Computed Tomography" in The Essential Guide to Image Processing; (Second Edition). A.Bovik (editor) Academic Press. Chapter 26, pp. 741-776, 2009.

[34] H. H. Barrett "Dipole sheet transform" *J. Opt. Soc. Am.* vol. 73, pp. 468-475, 1982.

[35] R. Clack, M. Defrise. "Overview of reconstruction algorithms for exact cone-beam tomography" Proc. of the SPIE: Mathematical Methods in Medical Imaging III. SPIE, Bellingham. 2299, 230-241, 1994.

[36] S. Bartolac, R. Clackdoyle, F. Noo, J. Siewerdsen, D. Moseley, D. Jaffray "A local shift-variant Fourier model and experimental validation of circular cone-beam computed tomography artifacts" *Med. Phys.* vol. 36, pp. 500-512, 2009.

[37] L. A. Feldkamp, L. C. Davis, J. W. Kress, "Practical cone-beam algorithm" *J. Opt. Soc. Amer. A*, vol. A6, pp. 612-619, 1984.

[38] G. T. Gullberg, G. L. Zeng, F. L. Datz, P. E. Christian, C.-H. Tung, H. T. Morgan, "Review of convergent beam tomography in single photon emission computed tomography" *Phys. Med. Biol.* vol. 37, pp.507-534, 1992.

[39] M. Bocher, I. M. Blevis, L. Tsukerman, Y. Shrem, G. Kovalski, L. Volokh "A fast cardiac gamma camera with dynamic SPECT capabilities: design, system validation and future potential" *Eur. J. Nucl Med Mol Imaging* vol 37, pp.1887-1902, 2010.

[40] L. Imbert, S. Poussier, P. R. Franken, B. Songy, A. Verger, O. Morel, D. Wolf, A. Noel, G. Karcher, P.-Y. Marie, "Compared Performance of High-Sensitivity Cameras Dedicated to Myocardial Perfusion SPECT: A comprehensive Analysis of Phantom and Human Images" *J. Nucl. Med.* vol. 53, pp.1897-1903, 2012.

[41] I. Loris, C. Verhoeven, "On a generalization of the iterative softthresholding algorithm for the case of non-separable penalty" *Inv. Prob*. 27: 125007 (15pp), 2011.

[42] I. Daubechies, M. Defrise, C. De Mol "An iterative thresholding algorithm for linear inverse problems with sparsity constraint" *Comm. Pure Appl. Math.* vol LVII, pp 1413-1457, 2004.

[43] M. Li, H. Yang, H. Kudo, "An accurate iterative reconstruction algorithm for sparse objects: applications to 3D blood vessel reconstruction from a limited number of projections" *Phys. Med. Biol.* vol. 47, pp.2599-2609, 2002.

[44] F. Noo, R. Clack, "Digital Radiography and Computed Tomography Algorithm Development and Implementation: Cone-beam Reconstruction Software Documentation and Instructions for User. INEL internal report, Idaho, November 19, 1996 (12 pages).

[45] F. Noo, "Méthodes numériques directes de reconstruction d'images tridimensionnelles à partir de projections coniques, Ph.D. Dissertation, Université de Liège, Belgium, 1998.

[46] S. G. Cuddy-Walsh, R. Clackdoyle, R. G. Wells, "Directional resolution of limited-angle multi-pinhole SPECT cameras" in Conference Record of the 2014 IEEE Nuclear Science Symposium and Medical Imaging Conference, November 8-15, 2015, Seattle. (4 pages)